Università degli Studi di Perugia

Dipartimento di Ingegneria

Tesi di Laurea Magistrale in Ingegneria Elettronica per L'Internet of Things

Numerical calibration of the bead-pull measurement setup for beam coupling impedance evaluation

Relatore:

Prof. Daniele Passeri

Correlatore:

Dr.ssa Arianna Morozzi

Supervisore esterno:

Dr. Carlo Zannini

Candidato:

Dalia Mahmoud Fouda El Dali

Matricola: **327650**

Anno Accademico 2021/2022

CERN-THESIS-2022-189 //2022

Abstract

To identify the accelerator structures that are contributing to performance limitations and execute mitigation techniques, a precise estimate of the beam coupling impedance is required. The beam coupling impedance of a device should ideally be assessed by activating it with the beam itself. However, in most circumstances, this solution is not practicable, and additional approaches must be used to analyze the influence of the beam. A well-known approach is to replicate the beam by feeding a current pulse via a wire stretched along the beam axis. The stretched wire method is a popular and well-liked method for determining beam coupling impedance. Yet, because the introduction of the stretched wire perturbs the EM boundary conditions, the information obtained from wire measurements may not exactly represent the answer to our initial dilemma. The existence of another conductive medium in the center of the device under investigation has the most obvious effect of allowing TEM propagation across the device with zero cut-off frequency. The existence of a TEM mode among the EM issue solutions will have the unintended consequence of causing extra losses. The modeling of the beam coupling impedance of complicated or rounded-shaped accelerator parts is difficult, and other methods are needed. The Bead-Pull method is a popular electromagnetic field measuring technique for tuning an RF cavity to meet design criteria. A tiny dielectric or metallic bead is drawn through a cavity while electric field measurements are obtained. Inserting a metallic or dielectric bead into a resonant cavity alters its frequency. This frequency shift is proportional to the sum of the squared amplitudes of the electrical and magnetic fields at the bead's position. The magnitude of the perturbation for a particular electromagnetic field is solely determined by the geometry of the perturbing item. As a result, calibration of the bead may be performed in a variety of resonant topologies without sacrificing generality. A method for doing precise bead calibration using electromagnetic simulations is proposed in this study. In comparison to the conventional technique of measuring a reference cavity, the simulation method's flexibility in studying alternative bead shapes and sizes may be useful in optimizing the measurement setup. A calibrated bead-pull configuration allows you to measure the electric field and hence the shunt impedance of the cavity's resonant modes. The beam coupling impedance obtained with the calibrated bead-pull arrangement is compared with well-established electromagnetic models.

Acknowledgment

Firstly, I would like to thank Dr. Carlo Zannini for offering me this unique opportunity and for giving me the opportunity to work in one of the biggest laboratories for scientific research in the world, the CERN. His advice as well as his reliability gave me the support I required to pursue my ideas, to trust my abilities and motivated me to a continuous effort to always obtain new aims on accelerator research studies

My heartfelt gratitude goes to my University supervisor, Prof. Daniele Passeri, for having always believed in my skills since I was in the Bachelor studies and for having helped me to reach my goals. His unique way of supervision and guidance encouraged me to push through discouragements and external odds.

My sincere thanks go to my University co-supervisor, Dr.ssa Arianna Morozzi, for the help during my studies and internships. She not only taught me a lot but she become a figure for which I have extreme admiration.

A special acknowledgement goes to all the project collaborators, starting from the ADAM ones to the CERN and Perugia University ones. I would especially like to thank Stefano Fanella for the help during the measurements.

Finally thank you to all the people with whom I shared so many experiences and memories during these years from Perugia to Geneva.

Contents

List of Tables

List of Figures

Introduction

This dissertation work was the result of a collaboration between the University of Perugia, CERN (Conseil européen pour la recherche nucléaire) and ADAM SA (Applications of Detector and Accelerators to Medicine). It is part of the research activity of the BE-ABP-CEI (BEam-Accelerator Beam Physics-Coherent Effects and Impedance) section at CERN.
The Beams Department is at the heart of the CERN accelerator complex. Whether it is the design of new accelerators and facilities, responsibility for essential component building, or exploitation of the entire complex and technological infrastructure, the BE team plays a critical role in supplying the Physics community with world-class scientific equipment. The group is organized in five sections responsible for the hadron sources and linear accelerators, optics and single particle dynamics, coherent and incoherent collective effects throughout the CERN circular accelerators and the design and operation of lepton accelerators (e.g. CLIC) and test facilities (e.g. CTF3). Across all sections, the group is responsible for the development, deployment, maintenance and support accelerator physics computer codes. This includes improving our understanding of the underlying accelerator physics, building and installing new accelerator components to improve the machine's capabilities, and developing new methods and processes for operating the machines in ways and at levels that were not necessarily considered when the machines were designed.

High beam intensity is required for future high-energy particle physics research using accelerators. The parasitic interaction of the charged particle beam with its surroundings can degrade beam quality and restrict the peak intensity at which safe machine operation can be assured. The beam induces electromagnetic fields in the accelerator components that surround it, which influences particle motion and can trigger beam instabilities. Beam coupling impedance is a concept that is widely used to characterize this interaction. With such high intensities, collective effects, where collective refers to the influence of the ensemble (all the particles) on a test particle, may provide a

performance constraint and be a crucial concern for the accelerator. Examples of collective effects are space charge or beam-beam effects, vacuum and electron cloud issues, and, as treated in this thesis, beam coupling impedance. The issues are twofold: longitudinal and transverse impedance can induce instabilities and unwanted tune changes, and the actual part of longitudinal impedance causes power dissipation in the component. This may result in substantial heating at high intensities. Analytical calculations or numerical simulations may often be used to determine a component's beam coupling impedance. These two techniques, however, are challenging in some instances due to complicated geometries or unknown electromagnetic material properties, and additional information is necessary. Beam measurements often only provide a broad view of the machine or, at best, a list of high-impedance parts. Furthermore, the majority of such measurements necessitate the use of valuable beam time. Bench measurements, on the other hand, can be performed in the laboratory on portions or the whole component in the air.

The coaxial wire method is the norm for bench measurements of the beam coupling impedance on particle accelerator elements. It is assumed that the EM field distribution (TEM field) of a bunch of extremely relativistic beams is remarkably similar to that of a brief pulse on a coaxial line. Note that the presence of the wire always lowers the Q of high Q DUTs like a cavity and usually detunes the resonance frequency. The wire permits the exchange of EM energy between discontinuities for frequencies below waveguide cut-off which would not be the case without the presence of the wire. Cavity-like structures may be assessed in terms of loss factor or R/Q using the wire approach. A change in Q caused by the wire does not, to first order, influence the R/Q value for short gaps (gap length beam-pipe diameter) and a thin wire in a single cell cavity. However, there are documented instances when wire-based R/Q measurements on cavities produced readings that were >50% off from the accurate value determined via bead-pull or numerical modeling. The wire's matching is also a typical issue. Thus wire based longitudinal impedance studies on cavity-like objects are conceivable, but should not actually be suggested.

The electric and magnetic fields in a cavity are commonly determined using the Slater Bead-Pull measuring method [1]. The fundamental idea is to sample the field in the cavity by moving a perturbing object, a bead or needle for example, through the cavity's longitudinal axis, the axis of the beam and pipe. While the bead traverses the whole cavity, a change in the resonance frequency is seen. The concept of a calibrated bead-pull technique as a bench method for beam coupling impedance measurements will be presented in this document.

- Chapter 2 provides a broad introduction to the concept of beam coupling impedance and the physics behind the beam-wall interaction.
- Chapter 3 presents an overview of the bead-pull approach for impedance studies. Additionally, a strong emphasis is placed on the necessity of calibrating the perturbing item used in the measurement already in simulations.
- Chapter 4 deals with the definition of the features of the measurement system. The emphasis is on specific factors, such as the various bead geometries and materials and how these impact the system's accuracy. The comparison of numerical simulation of the DUT with measurements will also be discussed in this chapter.

Chapter 1

CERN: Conseil européen pour la recherche nucléaire

1.1 Particle Accelerators

Particle accelerators were originally designed to provide beams for nuclear and particle research, fulfilling various needs in terms of beam intensity, energy, as well as particle types. Many more uses of particle accelerators were then found, ranging from industrial applications to particle therapy for cancer treatment. Charged particles, such as protons or electrons, are propelled at high speeds near the speed of light by an accelerator. Electric fields are employed in particle accelerators to accelerate and raise the energy of a stream of particles that is directed and focused by magnetic fields. The particles to be accelerated, such as protons or electrons, are supplied by the particle source. In the metal beam pipe, a particle beam moves inside a vacuum. The vacuum is essential for maintaining air and dust-free environment in which the particle beam may flow freely. Electromagnets guide and concentrate the particle beam as it goes through the vacuum tube. At a specific frequency, electric fields around the accelerator transition from positive to negative, producing radio waves that accelerate particles in groups. They are subsequently crushed against other particles flowing in the opposite direction or against a target.
Particle accelerators can be classified into three main categories:

- Linear accelerator (often shortened to Linac) [6] boosts charged subatomic particles or ions to high speeds by passing them through a sequence of oscillating electric potentials along a linear beam-line. The majority of accelerators employ some type of radio-frequency (RF)

acceleration because electrostatic breakdown restricts the highest constant voltage that can be delivered across a gap to generate an electric field. In RF acceleration, a voltage source is used to move the particle through a sequence of accelerating zones such that the particle may see an accelerating field as it passes through each one. Particles must inevitably move in "bunches" during this sort of acceleration, which corresponds to the period of the oscillator's cycle where the electric field is pointing in the direction of acceleration. The small accelerations add together to give the particles greater energy than could be achieved by the voltage used in one section alone. The design of a Linac depends on the type of particle that is being accelerated.

- Cyclotron accelerates charged particles outwards from the center of a flat cylindrical vacuum chamber along a spiral path.[9] The particles are held to a spiral trajectory by a static magnetic field and accelerated by a rapidly varying electric field. In a linear particle accelerator, in order for a bunch to "see" a forward voltage every time it crosses a gap, the gaps must be placed further and further apart, in order to compensate for the increasing speed of the particle. A cyclotron, by contrast, uses a magnetic field to bend the particle trajectories into a spiral, thus allowing the same gap to be used many times to accelerate a single bunch. As the bunch spirals outward, the increasing distance between transits of the gap is exactly balanced by the increase in speed, so a bunch will reach the gap at the same point in the RF cycle every time.

- Synchrotron is a form of cyclic particle accelerator derived from the cyclotron in which the accelerating particle beam follows a set closed-loop route. [10] While a classical cyclotron implements both a constant guiding magnetic field and a constant-frequency electromagnetic field (and thus operates in the classical approximation), its successor employs local variations in the guiding magnetic field to adapt to the increasing relativistic mass of particles during acceleration. This adaptation is accomplished by varying the magnetic field intensity over time rather than in space. The frequency of the applied electromagnetic field may also shift to follow the non-constant circulation time of particles that do not travel at the speed of light. By adjusting these parameters as the particles gain energy, the circulation route may be kept constant while they accelerate. This enables the particle vacuum chamber to be a huge thin torus rather than a disk as in prior, com-

pact accelerator designs. Furthermore, the vacuum chamber's small profile allowed for more efficient utilization of magnetic fields than in a cyclotron and since bending, beam focusing, and acceleration can be divided into independent components, the synchrotron was one of the first accelerator designs to permit the building of large-scale facilities.

Beams of high-energy particles are useful for fundamental and applied research in the sciences, and also in many technical and industrial fields unrelated to fundamental research. Physicists can examine the realm of the endlessly small by investigating the collisions between particles or between particles and targets. When the particles are sufficiently energetic, an incredible thing occurs: the collision's energy is turned into the matter in the form of new particles, the most massive of which existed in the early Universe. Einstein's famous equation $E = mc^2$ describes these phenomena, stating that matter is a concentrated form of energy, and the two are interchangeable. Over the past years, technological progression has allowed an increased performance of particle accelerators, leading to important discoveries. This is why particle accelerators and colliders such as the Large Hadron Collider (LHC) operated by CERN are used in particle physics.

1.2 CERN and the CERN accelerator complex

At the end of the Second World War, European science was no longer world-class. Following the example of international organizations, a handful of visionary scientists imagined creating a European atomic physics laboratory. Raoul Dautry, Pierre Auger and Lew Kowarski in France, Edoardo Amaldi in Italy and Niels Bohr in Denmark were among these pioneers. Such a laboratory would not only unite European scientists but also allow them to share the increasing costs of nuclear physics facilities. The first meeting of the CERN Council quickly followed the signing of the agreement. The draft convention was completed in the alotted 18 months and approved unanimously by the representatives of the eleven countries that had signed the original agreement plus the UK, and the document was made available for signature. At the sixth session of the CERN Council, which took place in Paris from 29 June - 1 July 1953, the convention establishing the organization was signed, subject to ratification. On 29 September 1954, following ratification by France and Germany, the European Organization for Nuclear Research officially came into being.

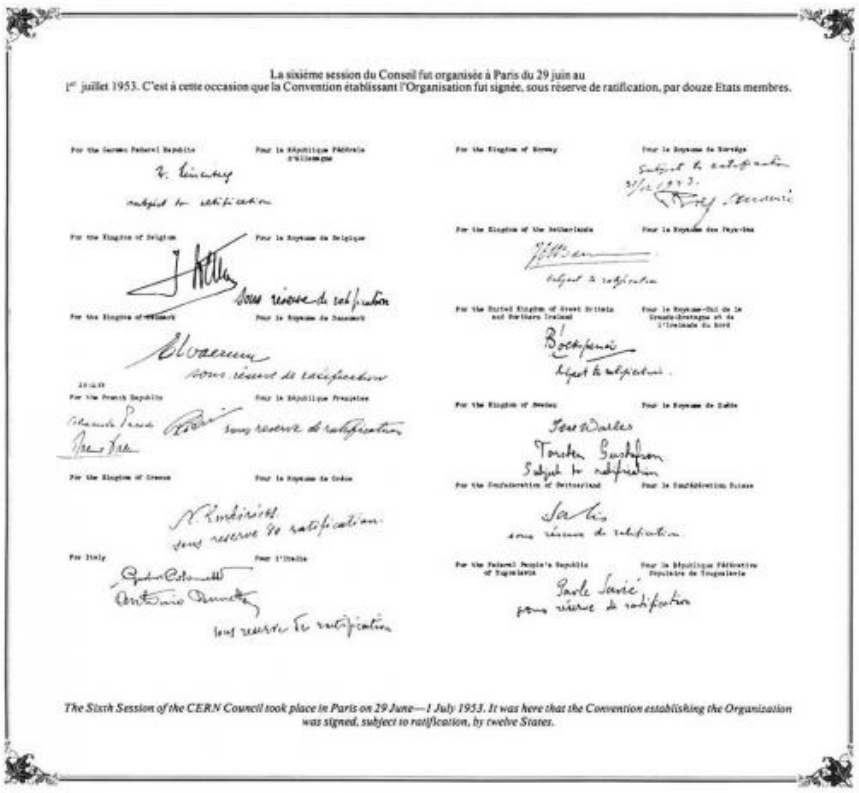

Figure 1.1: The European Organization for Nuclear Research was founded in 1954 by 12 European states.

It aimed to rebuild the European nuclear physics landscape which had been shattered by the Second World War and share the increasing cost of research instruments among its members. CERN has developed a number of policies and official documents that enable and promote open science, starting with CERN's founding convention in 1953 which indicated that all its results are to be published or made generally available.Since then, CERN published its open access policy in 2014 which ensures that all publications by CERN authors will be published with gold open access and most recently an open data policy that was endorsed by the four main LHC collaborations (ALICE, ATLAS, CMS and LHCb). The organization's role within the open science landscape is strongly affirmed by stating: "The particle physics community should work with the relevant authorities to help shape the emerging consensus on open science to be adopted for publicly-funded

research, and should then implement a policy of open science for the field". [12] The open data policy complements the open access policy, addressing the public release of scientific data collected by LHC experiments after a suitable embargo period. Its primary mission is to provide particle accelerators and other infrastructure required for high-energy physics research; as a result, various experiments have been built at CERN through multinational collaborations. Since researchers require remote access to these resources, the lab has historically served as a key wide area network hub. CERN is also the origin of the World Wide Web. Indeed, based on the concept of hypertext, the project was originally conceived and developed to meet the demand for automated information-sharing between scientists in universities and institutes around the world. The first website was activated in 1991. On 30 April 1993, CERN announced that the World Wide Web would be free to anyone. A copy of the original first webpage, created by Berners-Lee, is still published on the World Wide Web Consortium's website as a historical document.

CERN operates a network of eight accelerators and two decelerators, and some additional small accelerators. Each machine in the chain increases the energy of particle beams before delivering them to experiments or to the next more powerful accelerator (the decelerators naturally decrease the energy of particle beams before delivering them to experiments or further accelerators/decelerators). The first accelerator, the Synchro-Cyclotron (SC), accelerated its first beam in 1957, but a second accelerator, the Proton Synchrotron (PS) was already under construction. While the SC was shut down in 1990, the PS still runs after 60 years of operation and delivers beams to fixed target experiments as well as to the Large Hadron Collider (LHC).
As high energy physics required larger instruments to reach higher energies, a 7 km long accelerator was designed. In 1976, the Super Proton Synchrotron was inaugurated. Five years later, it was converted to a proton-antiproton collider, leading to the discovery of the W and Z bosons. As the understanding of the standard model progressed further, the energy reached by colliders became insufficient to explore rare phenomena. In consequence, CERN designed in the 1980s the 27 km long Large Electron Positron (LEP) collider. The LEP helped further investigate the properties of the W and Z bosons discovered beforehand in the SPS. At the beginning of the 2000s, the LEP was dismantled to make room for the LHC. From the beginning, the LHC design foresaw the use of cutting-edge technologies: 8 T superconducting magnets to guide the beam along the 27 km ring. The two counter-rotating beams are kept separate from one another, requiring twin-aperture magnets and they are accelerated by superconducting radio-frequency cavities. The

magnets cold bore are maintained at ≈2 K with a flow of super-fluid helium created by large cryogenics plants. Of course, the LHC is the last element of the vast complex of CERN accelerators:

1. After the proton source, a linear accelerator, the Linac 2, regroups the protons in bunches and accelerates them up to kinetic energy of 50 MeV.

2. The Proton Synchrotron Booster (PSB) accelerates the proton beams from 50 MeV to 1.4 GeV kinetic energy. It is also in the Booster that the proton bunches' intensities and transverse sizes are defined.

3. The Proton Synchrotron accelerates the beams from 1.4 GeV to 26 GeV. The PS is also a key accelerator: thanks to its various RF systems, one bunch can be split into multiple bunches, and they can be merged or shortened to provide finely tuned beams for the SPS and the LHC.

4. The Super Proton Synchrotron is the last stage before the LHC: the bunches are accelerated from 26 GeV to 450 GeV.

The accelerator complex serves not only the LHC but also a rich and diverse experimental program. Most of the other accelerators in the chain have their own experimental halls where beams are used for experiments at lower energies, serving fixed target experiments or antimatter production. Operation with ion beams is also possible and involves additional accelerators, the Linac 3 and the Low Energy Ion Ring (LEIR) at the beginning of the chain. Furthermore, other experiments require antiproton or heavy-ions beams. The PSB serves the Online Isotope Mass Separator (ISOLDE). The PS serves the Antiproton Decelerator, the neutron time-of-flight (n_TOF) facility, and an experimental area known as the East Area, which houses the CLOUD experiment as well as IRRAD and CHARM. The SPS serves the North Area experiments COMPASS, NA61/SHINE, NA62, NA63, NA64 and UA9, as well as the CERN Neutrino Platform, AWAKE and HiRadMat. The LHC serves four large experiments, ALICE, ATLAS, CMS and LHCb, as well as the smaller TOTEM, LHCf, MoEDAL and FASER experiments.CERN, in collaboration with groups worldwide, is also investigating two main concepts for future accelerators: a linear electron-positron collider with a new acceleration concept to increase the energy (CLIC) and a larger version of the LHC, a project currently named Future Circular Collider.

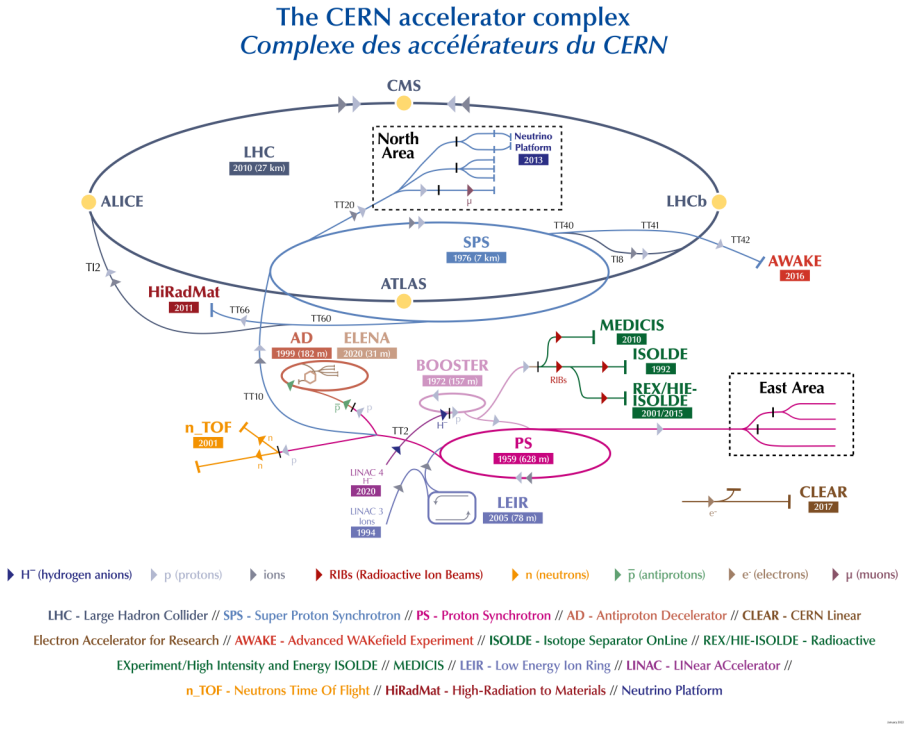

Figure 1.2: The CERN accelerator complex.

Chapter 2

Beam Coupling Impedance

The Lorentz force created by the "external" electromagnetic fields generated by the guiding and focusing magnets, RF cavities, and other key accelerator equipment has a low-intensity effect on a beam of charged particles traveling around an accelerator. When the beam intensity rises, the beam can no longer be seen as a collection of independently moving single particles. The term "collective effects of beam dynamics" refer to a group of events where the evolution of the beam depends on the interaction of the beam's particles with external fields. This interaction may cause significant issues with accelerator operation, such as overheating of vacuum chamber components or unstable beam motion, which may degrade the beam quality or restrict the beam's intensity. Depending on the nature of engagement, these effects can be divided into many categories:

- Space Charge Effects resulting from the Coulomb interaction between beam particles;
- Wakefields Effects resulting from the beam's contact with its surroundings;
- Beam-Beam Effects effects due to interaction of the beam with the contrarian beam in a collider
- Electron Cloud Effects due to the interaction between beam and electrons produced in the accelerator structure

All these disturbances in longitudinal and transverse planes result in a very significant problem for particle accelerators. Impedance is a term used to describe how a particle beam interacts with its environment. In essence, the

interaction intensity is inversely proportional to the product of the beam current and impedance. To put it more properly, a beam moving through a complicated vacuum chamber triggers charges and currents in the structures it passes through, creating electromagnetic fields that are more specifically referred to as wake fields. The particle beam's tail and velocity are both impacted by the E.M. fields produced by the head of the beam, which leads to beam dynamics instability. A result of this is that an accelerator may be thought of as a feedback mechanism, where any longitudinal or transverse perturbation in the beam distribution may be amplified or damped by the E.M. forces produced by the disturbance itself. When the beam intensity in an accelerator approaches greater levels, the impact becomes significant. In reality, the beam motion is started and allowed to expand, and in the absence of any damping device, the beam is soon deteriorated or even lost. Furthermore, the beam's energy is eventually dissipated as heat in the accelerators' equipment, potentially causing damage. All of these "perturbations" and their underlying causes should be correctly measured as the beam intensity increases, by examining the motion of the charged particles using the total electromagnetic fields, which are the sum of the external and perturbation fields.

For decades, beam instabilities have been the focus of a significant investigation. As the machine's performance increased, additional processes were identified, and the current problem is to analyze the interactions between all of these events because it is not always possible to treat the different impacts individually. In this specific case, studying the impedance is a crucial component of the accelerator design for a new accelerator project since it allows identifying possible mitigation techniques, ensuring beam stability during operations, and reducing beam-induced heating. To achieve success, the impedance must be reduced without compromising the device's functionality. This thesis pays special attention to the beam coupling impedance seen as the Fourier transform of the wakefield. The word "wake" refers to the fact that the causality principle forbids the existence of an electromagnetic field in front of the beam in the ultra-relativistic limit.

2.1 Wake functions and wake potential

The wake function is a Green's function that describes how a single source charge q_1 applies a force on a test charge q_2, both directly and indirectly by interference with the (lossy) wall, see Fig. 2.1. The relevant quantity for both beam dynamics and heat load considerations is the integrated force, i.e.

the energy or momentum change, rather than at the instantaneous values. This integrated force is determined by the relative distance s between q_1 and q_2 as well as their transverse locations, rather than by time or longitudinal position.

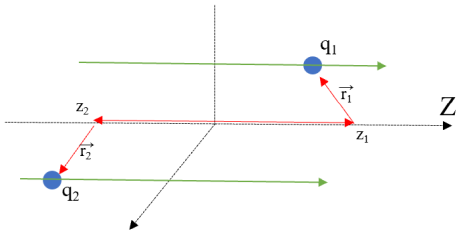

Figure 2.1: Longitudinal cut through an accelerator structure and centered coordinate system. The charge q_1 is usually referred to as source or leading charge and q_2 is referred to as test or trailing charge.

In Fig. 2.1 there is a source particle $q_1(z_1,\ r_1)$ and a test particle $q_2(z_2,\ r_2)$ traveling with constant velocity $v = \beta c$, where c is the speed of light in vacuum and β is the relativistic factor. The Lorentz the force generated by the source particle q_1 and acting on the test particle q_2 is:

$$\mathbf{F} = q[\mathbf{E} + \mathbf{v} \times \mathbf{B}] = q[E_z\hat{z} + (E_x - vB_y)\hat{x} + (E_y + vB_x)\hat{y}] = \mathbf{F}_{\parallel} + \mathbf{F}_{\perp} \quad (2.1)$$

The electromagnetic fields $\mathbf{E}$ and $\mathbf{B}$ generated by the charge q_1 in the structure may be calculated by solving the Maxwell equations imposing the appropriate boundary conditions.

$$\nabla \times \mathbf{B} = \mu_0 \mathbf{j} + \frac{1}{c^2}\frac{\delta \mathbf{E}}{\delta t} \qquad \nabla \cdot \mathbf{B} = 0 \quad (2.2)$$

$$\nabla \times \mathbf{E} = -\frac{\delta \mathbf{B}}{\delta t} \qquad \nabla \cdot \mathbf{E} = \frac{1}{\epsilon_0}\rho \quad (2.3)$$

where ρ is the Gaussian charge distribution, j is the corresponding current density, and μ_0 ϵ_0 are the constants of magnetic permeability and electrical permittivity respectively.
The Lorentz force is made up of two components, $F_{\parallel}$ is the longitudinal force that affects the energy of the test particle, and $F_{\perp}$ is the transverse force that deflects its trajectory. Typically, two assumptions are used to decouple the equations of motion from electromagnetism:

1. Rigid Beam Approximation: Although the leading charge loses energy, its velocity remains unchanged. I.e. the wakefield perturbation does not affect the motion of the beam during the traversal of the impedance. The distance z of the test particle behind some source particle does not change. This is exactly fulfilled for an ultra-relativistic beam that carries infinite energy.

2. Kick Approximation: The wake force continuously acting on the trailing charge is lumped in a single kick after the passage through the device. This means that can be considered the impulse instead of the force point by point.

These assumptions are confirmed by the different time scales of particle passage (fast) and the emergence of wakefield effects (slow). The wake function is defined as follows:

$$\mathbf{W}(\mathbf{r}_2^{\perp}, \mathbf{r}_1^{\perp}, s) := \frac{1}{q_1 q_2} \int_{-\infty}^{\infty} \mathbf{F}\Big(\mathbf{r}_2, z_2, t\Big) dz_2 = \frac{1}{q_1} \int_{-\infty}^{\infty} [\mathbf{E} + \mathbf{v} \times \mathbf{B}]\Big(\mathbf{r}_2, z_2, t\Big) dz_2 \tag{2.4}$$

In this way, a positive number implies momentum or energy gain for the test charge. The integral (Eq.2.4) existed only if the hypothesized infinitely long pipe connections do generate wakefields, which necessitates the following conditions:

- No smooth pipe (geometric wakefields)
- No perfectly conducting pipe (resistive wakefields)
- No beam with ultra relativistic properties (space charge wakefields)

Because the dispersed fields from the 3D region diminish in the pipe, the infinite integration in Eq.2.4 may be replaced by a finite one when all of these requirements are met.
The energy variation is defined as the integrated longitudinal force acting on the test particle along the structure. Considering a device of length L, it is expressed as follows:

$$U(r_2, r_1) = \int_0^L \mathbf{F}_{\parallel} ds \approx U(z) \tag{2.5}$$

The longitudinal wake function is the energy loss normalized by the two charges of the particles:

$$w_{\parallel}(z) = -\frac{U(z)}{q_2 q_1} \qquad [V/C] \tag{2.6}$$

The transverse placements have no effect on the longitudinal wake function (Eq.2.6). The wake function can be enlarged in multipolar terms in the case of symmetric structures, particularly those with cylindrical symmetry and ultra-relativistic charges. The first term is the main term in the longitudinal situation, and the wake function is simply dependent on z [7]. Furthermore, it is a convention to add a negative sign to obtain a positive wake for a decelerating field.
It is also necessary to include the following loss factor:

$$k = -\frac{U(z=0)}{q_2^2} \tag{2.7}$$

which is the energy lost by the source particle per unit charge squared. We can clearly see from the formulae above that when the charges follow the same trajectory, the loss factor is the wake function in the case of zero distance between q_2 and q_1: $k = w_z(0)$. This is true in the case of β <1, while the beam loading theorem, which states:

$$k = \frac{w_{\parallel}(z \to 0^+)}{q_2^2} \tag{2.8}$$

It indicates that an ultra-relativistic particle can only observe half of its own wake and can only exist in the z <0 area. The electromagnetic energy of modes that propagate down the beam chamber (above cut-off), which will eventually be wasted on surrounding lossy materials, and the electromagnetic energy of modes that stay trapped in the accelerator devices, are two components of the energy lost by the source. In the latter, this energy can be wasted on the lossy walls or continue to ring without damping, but it can also be passed to subsequent particles, potentially feeding into instability. A positive transverse wake indicates a defocusing transverse force. The transverse wake functions, like the longitudinal wake functions, may be expanded into a power series in the offset of the source and test particle. Because no transverse effects may occur when the source and test particles are at the center of symmetry, the power series' zeroth order term is null. Due to the ultra-relativistic approximation, the wake also vanishes in the transverse case for z > 0.

2.1.1 Wake potential

Because it is created by a point charge, the wake function stated in Eq. 2.6 is a Green function. When a bunch of particles moves parallel to the axis at r_1, its wakefields can still be estimated using the wake function of the point charge for any bunch distribution. Indeed, when the longitudinal plane and a bunch with longitudinal distribution $\lambda(z)$ are considered, the wake function created by the bunch distribution at a location z is simply provided by the convolution of the Green function over the bunch distribution. In practice, the superposition concept is used to calculate the convolution integral. The distribution is divided into an unlimited number of tiny slices, with their wake contributions totaled at the point *z'*. According to the definitions given so far, the wake potential of a bunch is expressed as follows:

$$W_{\parallel}(z) = \frac{1}{Q}\int_{-\infty}^{z} w_{\parallel}(z'-z)\lambda(z')dz' \tag{2.9}$$

where Q is the total charge of the bunch. The same consideration can be done for the transverse plane, the transverse wake potential is:

$$W_{\perp}(z) = \frac{1}{Q}\int_{-\infty}^{z} w_{\perp}(z'-z)\lambda(z')dz' \tag{2.10}$$

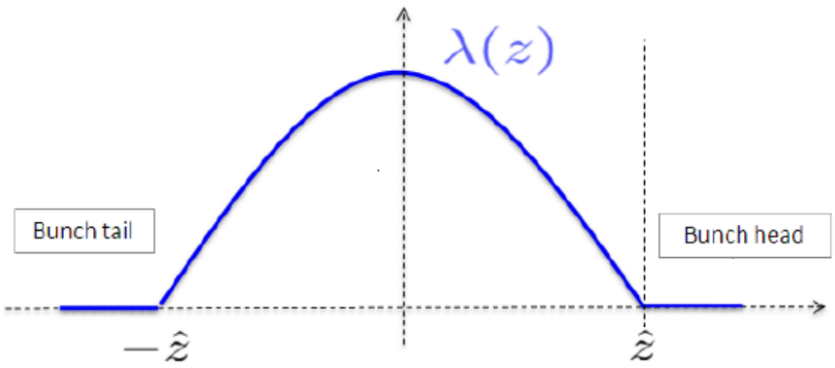

Figure 2.2: Bunch spatial distribution.

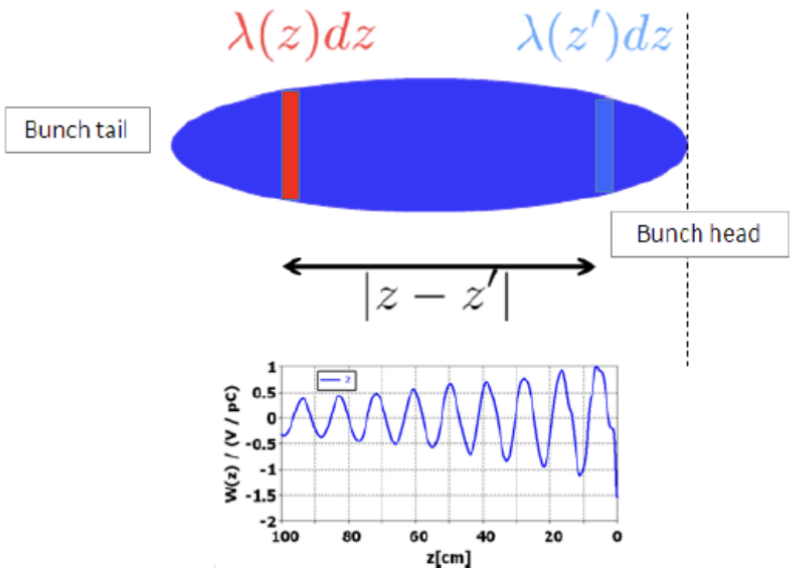

Figure 2.3: At the top, the slice view is the bunch. At the bottom, the wake is left behind each slice.

2.2 Relationship between longitudinal and transverse impedance

The equivalent of the wake functions in the frequency domain may be determined by applying its Fourier transform:

$$Z_{\parallel} = \frac{1}{c}\int_{-\infty}^{\infty} w_{\parallel}(e)^{j\frac{\omega z}{c}} dz \qquad [\Omega] \tag{2.11}$$

Here j is the imaginary unit and $\omega = 2\pi f$ is the angular frequency. In general, the beam coupling impedance is a complex quantity: $Z(\omega) = Z_r(\omega) + jZ_i(\omega)$. Where, for the longitudinal impedance $Z_r(\omega)$, $Z_i(\omega)$ are even and odd functions of ω, while for the transverse is the opposite.
The concept of an impedance in an electrical circuit is analogous to wakefields induced by a charged particle beam in an accelerator component. The beam acts as a time-varying current source, inducing voltage along the beam's pathway. As a result, the idea of beam coupling impedance, which connects the induced voltage to the beam current over the frequency spectrum, is presented. The impedance is highly important in analyzing the influence of different accelerator components on the beam and their contribution to an

accelerator's total impedance budget, which may not be exceeded to ensure stable operation for a given beam intensity. Similarly to the wake function, the beam coupling impedance might be calculated directly in the frequency domain using the current and field components [8].

Since the particles move at the fixed velocity $v = \beta c$ through the accelerating structure, an important quantity is the impulse, defined as follows:

$$\Delta p(x, y, z) = \int_{-\infty}^{\infty} \mathbf{F} dt = \int_{-\infty}^{\infty} q[\mathbf{E} + \mathbf{v} \times \mathbf{B}] dt \tag{2.12}$$

From the definition of the impulse can be introduced an important theorem which links the transverse and longitudinal impedance. Starting from the four Maxwell equations, for a particle in the beam, can be shown (considering $\beta = 1$):

$$\nabla \times \Delta p(x, y, z) = 0 \tag{2.13}$$

which is known as the Panofsky-Wenzel theorem [2]. This relation is very general, as no boundary conditions have been imposed. In principle it is sufficient to know the longitudinal wake potential for all transverse positions *(x,y)* or *(r,ϕ)* because it is possible to reconstruct the transverse component of the wake potential.

From the Maxwell equation $\nabla \times \mathbf{E} = -\frac{\delta}{\delta t}\ \mathbf{B}$ it's possible to obtain:

$$e_z \times \frac{\delta \mathbf{B}}{\delta t} = \frac{\delta \mathbf{E}_\perp}{\delta z} - \nabla_\perp \mathbf{E}_z \tag{2.14}$$

Since the total derivative of the transverse component of the electric field with respect to z is given by:

$$\frac{\delta}{\delta z}\mathbf{E}_\perp\Big(x, y, z, \frac{z+s}{c}\Big) = \Big(\frac{\delta}{\delta z} + \frac{1}{c}\frac{\delta}{\delta t}\Big)\mathbf{E}_\perp\Big(x, y, z, \frac{z+s}{c}\Big) \tag{2.15}$$

the derivative of the transverse wake potential with respect to s can be written as:

$$\frac{\delta}{\delta s}\mathbf{w}_\perp(x, y, s) = \frac{1}{q_2}\int_{-\infty}^{\infty}\Big((\frac{d}{dz}\mathbf{E}_\perp)(\mathbf{r}, \frac{z+s}{c}) - \nabla_\perp)\mathbf{E}_z(\mathbf{r}, \frac{z+s}{c})\Big)dz \tag{2.16}$$

A consequence of the Panofsky- Wenzel theorem is the following relationship:

$$\nabla_\perp w_\parallel(z) = \frac{\delta}{\delta z} w_\perp \tag{2.17}$$

Eq. 2.17 can link the longitudinal with the dipole transverse impedance by performing the Fourier transform.

2.3 Bench measurement of beam coupling impedance

The meticulous creation of an impedance budget for each particle accelerator design is a precondition for achieving desired performance. As a result, theoretical analysis, computer simulations, and actual measurements of accelerator components' beam coupling impedance are key jobs in accelerator research, design, and development. Computer simulations may be divided into three categories: Time Domain (TD), Frequency Domain (FD), and approaches without a particle beam. TD approaches are the most frequent since they simply require matrix-vector multiplications for time stepping. They are often based on Finite Differences Time Domain (FDTD) or Finite Integration Technique (FIT), which result in a Cartesian mesh discretization of a coincident space.

CST Studio Suite [13], a 3D electromagnetic Computer-Aided Design (CAD) application widely used for the computation of wakes and impedances, is the most often utilized software. Particle Studio's (PS) Wakefield solver, in particular, solves Maxwell's equations in the time domain utilizing a particle bunch as an excitation of the structure under investigation. The simulation produces the wake potential and the beam coupling impedance. The exciting Gaussian bunch, that is the source, generates the wake function as a function of the time delay with respect to the source's passage. It is the voltage gain of a unit charge passing the structure with a delay relative to the leading charge, caused by the latter's fields. The beam coupling impedance is the Fourier transform normalized to the bunch spectrum, or the frequency domain counterpart of the wake potential. In terms of experimental measurements, ideally, the beam coupling impedance of the accelerator components should be evaluated by activating the device with the beam itself. However, this strategy, which is in theory the best, is not always practical. Furthermore, when we require information on the behavior of the components prior to machine setup, bench measurements are desirable. The stretched Wire technique (WM) [8] is a popular alternative for measuring the beam coupling impedance of accelerator systems for this purpose. In frequency domain simulations, the WM is also a typical strategy for approximating beam excitation.

2.3.1 The Wire Method and its limits

Due to the sensitivity of the beam coupling impedance to the boundary conditions of the equipment used, it is necessary to utilize different measurement techniques to fully analyze the impedance of accelerator structures. The

coaxial wire approach [5], also known as the stretched wire method, is suited for structures that are predicted to have predominantly low Q-resonances. Sands and Rees initially introduced this approach in 1974 and nowadays it is widely used. In particular, at CERN, the method is employed to measure the longitudinal and transverse beam coupling impedance of a kicker in the frequency domain.
This method relies on the similarity of the electromagnetic field profile due to an ultra-relativistic charged particle and that of a short electrical pulse sent along a coaxial wire. A traveling charged particle generates an electromagnetic field in an arc transverse to its direction of motion, with the angle of the arc opening inversely equal to the particle's relativistic component. The field becomes completely perpendicular to the direction of motion for an ultra-relativistic particle ($\gamma \to \infty$). A short electrical pulse sent along the same path that the charged particle would take (in most cases, this is well represented by a straight wire) would propagate in the TEM (Transverse Electrical and Magnetic field) mode, producing a field profile similar to that emitted by the ultra-relativistic charged particle.

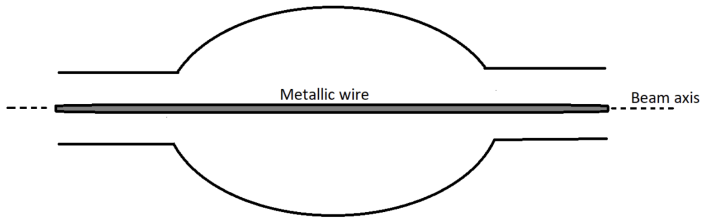

Figure 2.4: Thin metallic wire placed along the beam axis of a structure.

An accelerator component with a thin metallic wire on its beam axis can be considered as a two-port circuit, which can be characterized with a Network Analyzer. In particular, the transmission scattering parameters of the Device Under Test (DUT) and the reference beam pipe (REF) can be measured.
The experimental setup is sketched in Fig. 2.5. Firstly the external circuit (i.e. everything which is not the DUT such as VNA, cables, transition between connections, etc.) is matched to the characteristic impedance of the coaxial line inside the DUT.

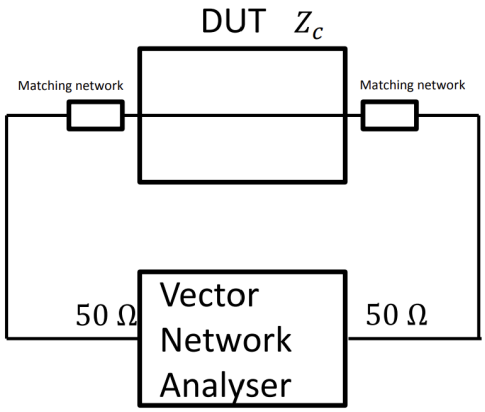

Figure 2.5: Experimental setup for a measurement of the beam coupling impedance using the classical coaxial wire method.

This is done by measuring the reflection coefficient Γ for the setup with only one port connected to the DUT and the other end terminated by an open connection. Knowing the characteristic impedance of the VNA and associated cables (typically $Z_{c0} = 50\ \Omega$), we can easily calculate the characteristic impedance of the DUT, Z_c, from the relation,

$$\Gamma = \frac{Z_c - Z_{c0}}{Z_c + Z_{c0}} \tag{2.18}$$

The characteristic impedance can then be electrically matched by connecting the DUT to the external circuit through a resistive network. This can be accomplished in two ways:

1. Adding resistors in series right before the DUT to resistively match the VNA and associated measurement setup's characteristic impedance (as viewed by the DUT) to that of the DUT, so that the series resistance $R_s = Z_c\text{-}Z_{c\ 0}$. An attenuator is frequently used to reduce the effect of reflections from the mismatch between the VNA and the resistor.

2. The use of two-way matching, with a parallel (R_p) and series (R_s) resistor. These resistance values are supplied by:

$$R_p = Z_{c0}\sqrt{\frac{Z_c}{Z_c - Z_{c0}}} \quad R_s = Z_{c0} - \frac{Z_c R_p}{Z_c + Z_{c0}} \tag{2.19}$$

The values that are wish to be measured to evaluate the beam coupling impedance of a device are the scattering parameters of the resulting circuit, in particular S21, the normalized transmission parameter through the DUT. The longitudinal beam coupling impedance of the DUT can be found as follows:

$$Z_{\parallel} = 2Z_{c0}(\frac{S_{21REF}}{S_{21DUT}} - 1) \tag{2.20}$$

Z_{c0} is the characteristic impedance of the equivalent transmission line formed by the wire and the DUT wall. In 1993, Vaccaro [8] derived a more rigorous and accurate formula, based on the transmission line theory. He showed that the longitudinal coupling impedance in a transmission line can be expressed by:

$$Z_{\parallel} = jZ_{c0}({k_{DUT}}^2 - {k_R}^2)\frac{l}{k_{REF}} \tag{2.21}$$

The k_{DUT} and k_{REF} are the propagation constant of the DUT and REF. If the line is matched implies $S_{11} = S_{22} = 0$ and $Z_c = Z_{ch}$ and in addition the propagation constant can be related to transmission coefficient by:

$$S_{21} = e^{-jkl} \tag{2.22}$$

and the longitudinal coupling impedance can be expressed as:

$$Z_{\parallel} = -Z_{c0}ln\frac{S_{21DUT}}{S_{21REF}}\Big(1 + \frac{lnS_{21DUT}}{lnS_{21REF}}\Big) \tag{2.23}$$

In most cases of the accelerator components, the S_{21DUT} is close to S_{21REF} and the formula can be approximated by the well-known Log-formula:

$$Z_{\parallel} = -2Z_{c0}ln\frac{S_{21DUT}}{S_{21REF}} \tag{2.24}$$

The Wire Method for Coupling Impedance Evaluations is intriguing because it allows for bench measurements as well as frequency domain simulations of beam excitation; in fact, scattering parameters and characteristic impedance are direct outputs of the simulations and experiments. Nonetheless, due to the existence of the wire, which perturbs the electromagnetic boundary conditions, this established approach has several drawbacks. In reality, the conductor in the structure's core affects its cross-section such that it is no longer simply connected, allowing the propagation of TEM modes with zero cut-off frequency. As a result, the WM may not fully represent the solution to our initial problem, resulting in extra losses during the measurements.

Chapter 3

Numerical Calibration of The Bead-Pull Method

Although the Wire Method is a well-established approach in the realm of particle accelerators, understanding its limits and developing new strategies to overcome them is a high-demand endeavor. In this respect, in addition to the difficulties discussed in paragraph 2.3.1, the focus has been narrowed down to feasible options that do not need a change of the DUT. The longitudinal beam coupling impedance is strongly bound to the transmission scattering characteristic since it is necessarily related to the energy loss of the electromagnetic wave traveling through the structure.
The simple example of a pill-box with resistive walls can clarify the reason. Let us consider a cavity mode below the cut-off frequency of the attached beam pipe. In the real configuration of the structure (without wire) this mode can only get dissipated on the cavity wall. By introducing a conductive wire, the beam pipe is turned into a coaxial cable and its cut-off frequency vanishes. The mode, which would be otherwise trapped in the cavity, will be able to lose power also through TEM propagation. Therefore, the quality factor measured with wire could be significantly lower than the actual quality factor of the mode (without wire) [11]. In this thesis, the bead-pull method is explored as a method to measure the beam coupling impedance of structures, avoiding the issue of the conductive wire.

3.1 Bead-Pull Method

The bead-pull method is a typical electromagnetic field measuring technique that is used to tune a radiofrequency cavity to meet design criteria and

create the appropriate accelerating field. A small dielectric or metallic bead is pushed through a cavity using a non-conducting wire while electric field measurements, from inside the structure itself, are collected. It is based on Slater's small signal perturbation theory [1], which claims that when a resonant cavity is perturbed by a small bead, whether metallic or dielectric, the resonant frequency varies from the initial frequency. This frequency shift $\Delta\omega$ is proportional to the combination of the squared amplitudes of the electrical and magnetic fields at the location of the bead. This relationship is given by the equation:

$$\frac{\Delta\omega}{\omega_0} = \frac{\omega - \omega_0}{\omega_0} = k \int_{\Delta r} \frac{\mu H^2 - \varepsilon E^2}{2U} dv = k_{SLH} \frac{|\ H\ |^2}{U} - k_{SLE} \frac{|\ E\ |^2}{U} \quad (3.1)$$

where ω and ω_0 are the new and the original resonant frequencies respectively, μ is the magnetic permeability, ε is the electrical permittivity, U is the energy stored in the cavity, k_{SLE} and k_{SLH} are constants determined by the shape and the material of the bead, while E and H are the electric and magnetic field amplitudes respectively. This equation shows that if the magnetic field or k_{SLH} is zero (as it is along the cavity's center), the electric field is precisely proportional to the change in the resonant frequency. As a result, if the resonant frequency changes, the electric field may be calculated by moving the bead along a line in the cavity.

The dimension of the perturbing object must be chosen so that the field does not vary significantly over its largest linear dimension and at the same time introduces a disturbance large enough to be distinguishable from the measurement noise. Shaped beads are used to enhance perturbation and give directional selectivity among different field components. For a given electromagnetic field, the amplitude of the perturbation depends only on the geometry of the perturbing object. Therefore, the calibration of the bead can be done in different resonant structures without loss of generality. In this thesis, a method to perform an accurate calibration of the bead with electromagnetic simulations is proposed. Compared to the common practice of measuring a reference cavity, the flexibility given by the simulation method to study different bead shapes and sizes could be advantageous to optimize the measurement setup. A calibrated bead-pull setup allows to quantify of the electric field and, therefore, the shunt impedance of the resonant modes of the cavity.

Bead-pull Radio Frequency (RF) measurements involve two types of perturbations:

1. Small material perturbation, like a small dielectric bead, enters a large volume of the cavity.

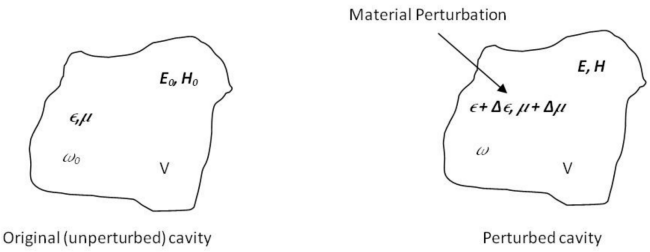

Figure 3.1: Material perturbation due to the introduction of a dielectric bead in the DUT.

2. Small cavity volume change, like a small metallic bead, enters a large volume of the cavity.

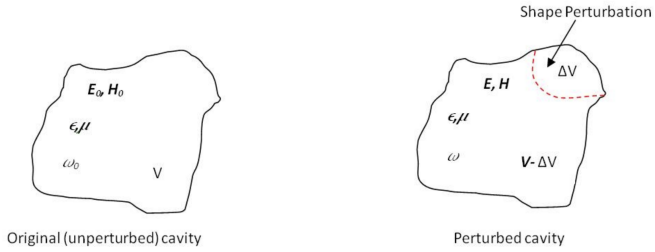

Figure 3.2: Volume perturbation due to the introduction of a metallic bead in the DUT.

Before the perturbation, the EM field inside of cavity can be described as:

$$E = E_0 e^{j\omega t} \qquad H = H_0 e^{j\omega t} \tag{3.2}$$

Here E_0 and H_0 are function of position before perturbation. Following the perturbation, the field gains two new values, E_1 and H_1 , and the resonance frequency is altered by a value $\Delta\omega$.

$$E' = (E_0 + E_1)e^{j(\omega+\Delta\omega)t} \qquad H' = (H_0 + H_1)e^{j(\omega+\Delta\omega)t} \tag{3.3}$$

Here $E_1 << E_0$ and $H_1 << H_0$ are the effect of small material perturbations or small volume changes. Taking into account the first and the second Maxwell's equation:

$$\nabla \times \mathbf{E} = -\frac{\delta \mathbf{B}}{\delta t} \tag{3.4}$$

$$\nabla \times \mathbf{H} = \frac{\delta \mathbf{D}}{\delta t} \tag{3.5}$$

Applying Eq.3.2 and Eq.3.3 to Eq.3.4:

$$\nabla \times \mathbf{E}_0 = -j\omega \mathbf{B}_0 \tag{3.6}$$

$$\nabla \times (\mathbf{E}_0 + \mathbf{E}_1) = -j(\omega + \Delta\omega)(\mathbf{B}_0 + \mathbf{B}_1) \tag{3.7}$$

It's possible to obtain:

$$\nabla \times (\mathbf{E}_0 + \mathbf{E}_1) = \nabla \times \mathbf{E}_0 + \nabla \times \mathbf{E}_1 = -j\omega \mathbf{B}_1 - j\Delta\omega(\mathbf{B}_0 + \mathbf{B}_1) \tag{3.8}$$

Similarly applying Eq.3.2 and Eq.3.3 to Eq.3.5:

$$\nabla \times \mathbf{H}_0 = j\omega \mathbf{D}_0 \tag{3.9}$$

$$\nabla \times (\mathbf{H}_0 + \mathbf{H}_1) = j(\omega + \Delta\omega)(\mathbf{D}_0 + \mathbf{D}_1) \tag{3.10}$$

It is feasible to get:

$$\nabla \times (\mathbf{H}_0 + \mathbf{H}_1) = \nabla \times \mathbf{H}_0 + \nabla \times \mathbf{H}_1 = j\omega \mathbf{D}_1 + j\Delta\omega(\mathbf{D}_0 + \mathbf{D}_1) \tag{3.11}$$

Multiplying H_0^* to Eq.3.8 and E_0^* to Eq.3.11:

$$\mathbf{H}_0^* \cdot \nabla \times \mathbf{E}_1 = -j[\omega \mathbf{H}_0^* \cdot \mathbf{B}_1 + \Delta\omega \mathbf{H}_0^* \cdot (\mathbf{B}_0 + \mathbf{B}_1)] \tag{3.12}$$

$$\mathbf{E}_0^* \cdot \nabla \times \mathbf{H}_1 = j[\omega \mathbf{E}_0^* \cdot \mathbf{D}_1 + \Delta\omega \mathbf{E}_0^* \cdot (\mathbf{D}_0 + \mathbf{D}_1)] \tag{3.13}$$

Evaluating the difference between Eq.3.13-Eq.3.12:

$$\begin{aligned} \mathbf{E}_0^* \cdot \nabla \times \mathbf{H}_1 - \mathbf{H}_0^* \cdot \nabla \times \mathbf{E}_1 = \\ j(\omega + \Delta\omega)(\mathbf{E}_0^* \cdot \mathbf{D}_1 + \mathbf{H}_0^* \cdot \mathbf{B}_1) + j\Delta\omega(\mathbf{E}_0^* \cdot \mathbf{D}_0 + \mathbf{H}_0^* \cdot \mathbf{B}_0) \end{aligned} \tag{3.14}$$

Now is it possible to use the vector differential operation and the Eq.3.6 and Eq.3.9 relationship to obtain:

$$\begin{aligned} \nabla \cdot (\mathbf{E}_0^* \times \mathbf{H}_1 - \mathbf{H}_0^* \times \mathbf{E}_1) = \mathbf{H}_1 \cdot \nabla \times \mathbf{E}_0^* - \mathbf{E}_0^* \cdot \nabla \times \mathbf{H}_1 + \mathbf{E}_1 \cdot \nabla \times \mathbf{H}_0^* + \\ \mathbf{H}_0^* \cdot \nabla \times \mathbf{E}_1 = j\omega(\mathbf{H}_1 \cdot \mathbf{B}_0^* + \mathbf{E}_1 \cdot \mathbf{D}_0^*) - (\mathbf{E}_0^* \cdot \nabla \times \mathbf{H}_1 - \mathbf{H}_0^* \cdot \nabla \times \mathbf{E}_1) \end{aligned} \tag{3.15}$$

This leads to:

$$\begin{aligned} \mathbf{E}_0^* \cdot \nabla \times \mathbf{H}_1 - \mathbf{H}_0^* \cdot \nabla \times \mathbf{E}_1 = \\ j\omega(\mathbf{H}_1 \cdot \mathbf{B}_0^* + \mathbf{E}_1 \cdot \mathbf{D}_0^*) - \nabla \cdot (\mathbf{E}_0^* \times \mathbf{H}_1 - \mathbf{H}_0^* \times \mathbf{E}_1) \end{aligned} \tag{3.16}$$

That can be applied to Eq.3.14:

$$\begin{aligned} j\omega(\mathbf{H}_1 \cdot \mathbf{B}_0^* + \mathbf{E}_1 \cdot \mathbf{D}_0^*) - \nabla \cdot (\mathbf{E}_0^* \times \mathbf{H}_1 - \mathbf{H}_0^* \times \mathbf{E}_1) = \\ j\omega(\mathbf{E}_0^* \cdot \mathbf{D}_1 + \mathbf{H}_0^* \cdot \mathbf{B}_1) + \\ j\Delta\omega[(\mathbf{E}_0^* \cdot \mathbf{D}_0 + \mathbf{H}_0^* \cdot \mathbf{B}_0) + (\mathbf{E}_0^* \cdot \mathbf{D}_1 + \mathbf{H}_0^* \cdot \mathbf{B}_1)] \end{aligned} \tag{3.17}$$

Integrating over the whole volume of cavity V_0 on both sides of Eq.3.17

$$\begin{aligned} j\omega \iiint_{V_0} [(\mathbf{E}_0^* \cdot \mathbf{D}_0 + \mathbf{H}_0^* \cdot \mathbf{B}_0) + (\mathbf{E}_0^* \cdot \mathbf{D}_1 + \mathbf{H}_0^* \cdot \mathbf{B}_1)] dv = \\ j\omega \iiint_{V_0} [(\mathbf{E}_1 \cdot \mathbf{D}_0^* - \mathbf{E}_0^* \cdot \mathbf{D}_1) + (\mathbf{H}_1 \cdot \mathbf{B}_0^* - \mathbf{H}_0^* \cdot \mathbf{B}_1)] dv - \\ \iiint_{V_0} \nabla \cdot (\mathbf{E}_0^* \times \mathbf{H}_1 - \mathbf{H}_0^* \cdot \mathbf{E}_1) dv \end{aligned} \tag{3.18}$$

According to the divergence theorem, the second term of the Eq.3.18 can become the surface integration on the cavity inner wall S_0 where E_0 and H_0 vanish:

$$\iiint_{V_0} \nabla \cdot (\mathbf{E}_0^* \times \mathbf{H}_1 - \mathbf{H}_0^* \cdot \mathbf{E}_1) dv = \iint_{S_0} \nabla \cdot (\mathbf{E}_0^* \times \mathbf{H}_1 - \mathbf{H}_0^* \cdot \mathbf{E}_1) ds = 0 \tag{3.19}$$

So Eq.3.18 becomes:

$$\frac{\Delta\omega}{\omega} = \frac{\iiint_{V_0} [(\mathbf{E}_1 \cdot \mathbf{D}_0^* - \mathbf{E}_0^* \cdot \mathbf{D}_1) + (\mathbf{H}_1 \cdot \mathbf{B}_0^* - \mathbf{H}_0^* \cdot \mathbf{B}_1)] dv}{\iiint_{V_0} [(\mathbf{E}_0^* \cdot \mathbf{D}_0 + \mathbf{H}_0^* \cdot \mathbf{B}_0) + (\mathbf{E}_0^* \cdot \mathbf{D}_1 + \mathbf{H}_0^* \cdot \mathbf{B}_1)] dv} \tag{3.20}$$

Equation 3.20 accurately expresses the change in cavity relative frequency brought on by the perturbations introduced by the bead-pull method on the distribution of the EM field. The second term in the denominator is close to zero since $\mid D1 \mid << \mid D0 \mid$ and $\mid B1 \mid << \mid B0 \mid$. Additionally, the values of E_1, D_1, H_1 and B_1 in volumes $V_0 - V_1$ (where V_1 is the volume of the cavity after the introduction of the bead) are essentially identical to their values in volumes V_0. Therefore, the volume integration in the numerator of Eq.3.20 can be roughly over volume V_1 alone.

$$\frac{\Delta f}{f} = \frac{\Delta\omega}{\omega} = \frac{\iiint_{V_1} [(\mathbf{E}_1 \cdot \mathbf{D}_0^* - \mathbf{E}_0^* \cdot \mathbf{D}_1) + (\mathbf{H}_1 \cdot \mathbf{B}_0^* - \mathbf{H}_0^* \cdot \mathbf{B}_1)] dv}{\iiint_{V_0} [(\mathbf{E}_0^* \cdot \mathbf{D}_0 + \mathbf{H}_0^* \cdot \mathbf{B}_0)] dv} \tag{3.21}$$

If V_1 is due to a metallic bead, inside the cavity it's possible to measure:

$$\mathbf{E}' = 0 \qquad \mathbf{D}' = \mathbf{D}_0 \qquad \mathbf{B}' = 0 \qquad \mathbf{H}' = \mathbf{H}_0 \tag{3.22}$$

Then the field variations inside the cavity are:

$$\mathbf{E}_1 = \mathbf{E}' - \mathbf{E}_0 = -\mathbf{E}_0 \qquad \mathbf{D}_1 = \mathbf{D}' - \mathbf{D}_0 = 0 \tag{3.23}$$

$$\mathbf{B}_1 = \mathbf{B}' - \mathbf{B}_0 = -\mathbf{B}_0 \qquad \mathbf{H}_1 = \mathbf{H}' - \mathbf{H}_0 = 0 \tag{3.24}$$

Applying Eq. 3.23 and 3.24 to Eq. 3.21, the cavity frequency change due to a metallic boundary perturbation is obtained:

$$\frac{\Delta f}{f} = \frac{\iiint_{V_1}[(\mathbf{H}_0^* \cdot \mathbf{B}_0 - \mathbf{E}_0 \cdot \mathbf{D}_0^*)dv}{\iiint_{V_0}(\mathbf{E}_0^* \cdot \mathbf{D}_0 + \mathbf{H}_0^* \cdot \mathbf{B}_0)]dv} \tag{3.25}$$

If V_1 is deformed in such a way that can be considered as a small perturbation, the new surface S_1 is parallel to the original surface S_0, then metallic boundary volume of δV:

$$\mathbf{B}_0 = \mu \mathbf{H}_0 \qquad \mathbf{D}_0 = \varepsilon \mathbf{E}_0 \tag{3.26}$$

$$\frac{\Delta f}{f} = \frac{\iiint_{\delta V}[(\mu \mid \mathbf{H}_0 \mid^2 - \varepsilon \mid \mathbf{E}_0 \mid^2)dv}{\iiint_{V_0}(\mu \mid \mathbf{H}_0 \mid^2 + \varepsilon \mid \mathbf{E}_0 \mid^2)]dv} \tag{3.27}$$

If V_1 is due to a dielectric object, the frequency change can be similarly obtained:

$$\frac{\Delta f}{f} = \frac{\iiint_{\delta V}[((\mu_r - 1)\mu_0 \mathbf{H}_1 \cdot \mathbf{H}_0^* - (\varepsilon_r - 1)\varepsilon_0 \mathbf{E}_1 \mathbf{E}_0^*]dv}{\iiint_{V_0}(\mu \mid \mathbf{H}_0 \mid^2 + \varepsilon \mid \mathbf{E}_0 \mid^2)]dv} \tag{3.28}$$

Both E and H field perturbations can cause the cavity frequency going down. A metallic bead is actually measuring both E and H fields inside a cavity.

1. To get an independent E and H field, one needs two types of bead, metallic and dielectric, by pulling them separately;

2. Pulling a dielectric bead with $\varepsilon_r > 1$, $\mu_r = 1$ is actually measuring E field only.

3. High material μ_r can be used to make a bead to measure the H field, but it might be under performed than a metallic bead

4. When $\varepsilon_r >> 1$ or $\mu_r >> 1$, E_1 and H_1 can not be approximated to zero.

3.2 Estimation of the accuracy of the simulations

As already mentioned in the preamble of Chapter 3, for a given electromagnetic field, the amplitude of the perturbation depends only on the geometry of the perturbing object. Therefore, the calibration of the bead can be done in different resonant structures without loss of generality. In this thesis, a method to perform an accurate calibration of the bead with electromagnetic simulations is proposed using a circular Pill-Box Cavity since it allows accurate studies due to its simplicity. A pill-box cavity is a specific type of cylindrical resonant cavity consisting of a closed metal structure, either hollow or filled with a dielectric material, that confines electromagnetic fields inside it, storing their energy. They are used to accelerate the particle beam. The cavity's walls serve as a rebounding surface for electromagnetic waves and in particular, standing wave fields are created when they reinforce one another at the cavity's resonance frequencies. In order to accelerate the particles that pass throughout the cavity, the electromagnetic field inside an RF cavity is the solution to the wave equation:

$$\left(\nabla^2 - \frac{1}{c^2}\frac{\delta^2}{\delta t^2}\right)\begin{Bmatrix} E \\ H \end{Bmatrix} = 0 \tag{3.29}$$

with the boundary conditions $\hat{n} \times E = 0$ and $\hat{n} \cdot H = 0$, where $\hat{n}$ is the unit vector normal to the surface. Solutions to Eq. 3.29 with the specified boundary conditions can be separated into two families of resonant modes with different eigenfrequencies, based on the direction of the electric and magnetic field:

- TE_{mnl} modes having only transverse electric fields, and
- TM_{mnl} modes having only transverse magnetic fields (but a longitudinal component of the electric field),

where n, m, l are the mode numbers in the θ, ψ, and z directions, respectively, in cylindrical coordinates. The magnetic field is concentrated near the cylindrical wall, which is responsible for RF losses and the electric field is concentrated near the axis, which is responsible for the acceleration. The resonant frequency of this mode can be calculated analytically for the pill-box geometry:

$$f_{nml} = \frac{c}{2\pi}\sqrt{\left(\frac{\rho_{nm}}{r}\right)^2 + \left(\frac{l\pi}{L}\right)^2} \tag{3.30}$$

Where:

- c is the speed of light;
- ρ_{nm} is the m-th zero of the Bessel's function of n-th order;
- r, L are the geometrical dimensions of the cavity.

The fundamental mode of a pill-box cavity is the TM_{010} mode, where $n = \rho = 0$ (azimuthal symmetry), $m = 1$ (no nodes of E_z with r), $l = 0$ (constant E_z in the z direction).

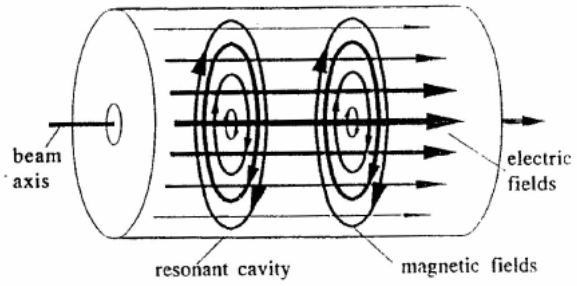

Figure 3.3: Electric and magnetic fields for the TM_{010} mode inside a pill-box cavity.

These modes have the electric field component directed along the axis of the cylinder and arise when the cavity is excited with particular frequencies. In particular, where $\rho = 0$ indicates that there is no axial field dependence—the eigenfrequency is actually the cutoff frequency of the TM_{010} mode of the round waveguide. The fields of the TM_{010} mode of the cavity are given by:

$$E_z = \frac{1}{j\omega_0\varepsilon_0}\frac{\rho_{01}}{r}\sqrt{\frac{J_0(\rho_{01}\frac{l}{r})}{\pi a J_1(\rho_{01})}} \qquad B_\varphi = \mu_0\sqrt{\frac{J_0(\rho_{01}\frac{l}{r})}{\pi a J_1(\rho_{01})}} \tag{3.31}$$

where J_0 and J_1 are Bessel functions of the zero-th and first order, respectively. Other resonant modes that are sometimes used are the TE_{011} mode and the TM_{110} mode. The first of these has a zero electric field on the cavity surface and is used to study the surface resistance of superconductors in RF magnetic fields. The second has a transverse component of the electric field on axis, tilting the beam, which is sometimes necessary in collider accelerators in order to provide a head-on collision between two beams and thereby increase the luminosity. The deflecting TM_{110} mode has also been used in a Superconductive RF separator cavity to separate beams of different types

of particles.[3]

The fields in the pill-box cavity can be given in the closed and exact form, but in the general case, the electromagnetic fields are calculated numerically by a number of specialized simulation programs that are commercially available. To perform simulations, a finite-element electromagnetic solver CST was used. This software allows to perform advanced simulations to characterize the electric and magnetic fields of a created model. To properly validate the analysis of the bead pull method is it necessary to estimate the accuracy of the simulation tool used to implement the model. Three domains of simulation have been explored:

- Eigenmode Solver is used to calculate the frequencies and the corresponding electromagnetic field patterns when no excitation is applied.
- Wakefield Solver calculates the so-called wake-potentials for a given structure from electromagnetic fields. Wakefield problems are driven by a bunch of charged particles, which is passing the observed structure parallel to a main coordinate axis. These particles cause electromagnetic fields, which are calculated with a time domain solver.
- Frequency Domain Solver: when a time-harmonic dependence of the fields and the excitation is assumed, Maxwell's equations may be transformed into the frequency domain. The frequency domain solver uses special broadband frequency sweep techniques in order to derive the full broadband spectrum from a relatively small number of frequency samples.

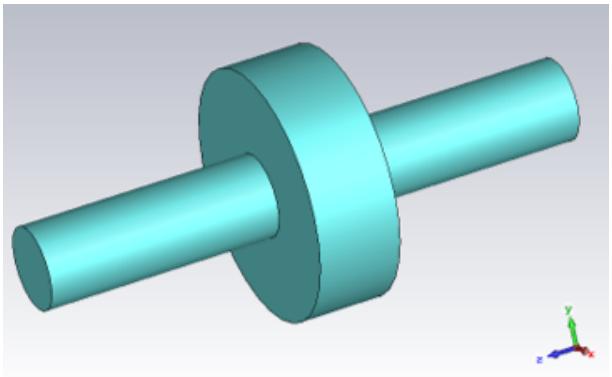

Figure 3.4: Pill-box cavity implemented in simulation.

The model used to evaluate the consistency of the simulation software is a pill-box cavity with $r = 90mm$, $L = 60mm$ and beam pipe of $l = 200mm$. A resonant cavity is characterized by its resonant frequency f_0, the quality factor of the resonance Q and its shunt impedance R.

3.2.1 Resonant Frequency

Resonant frequency is the oscillation of a system at its natural or unforced resonance. Resonance occurs when a system is able to store and easily transfer energy between different storage modes. In this simple case, some analytical results can be compared with the numerical ones. Recalling Eq.3.30 and using the values from Table 3.1:

ρ_{nm}		n				
		1	2	3	4	5
m	1	2.4048	3.8317	5.1356	6.3802	1 7.5883
	2	5.5201	7.0156	8.4172	9.7610	11.0647
	3	8.6537	10.1735	11.6198	13.0152	14.3725
	4	11.7915	13.3237	14.7960	16.2235	17.6160
	5	14.9309	16.4706	17.9598	19.4094	20.8269

Table 3.1: Zeros of Bessel's Functions.

It's possible to obtain the following table. [1]

Mode	CST (GHz)[1]	CST (GHz)[1]	CST (GHz)[1]	Analytical (GHz)
TM_{010}	1.3115	1.3111	1.3118	1.3049
TM_{110}	1.9606	1.9596	1.9596	1.9714
TM_{210}	2.6978	2.6940	2.6940	2.7126

Table 3.2: Comparison between analytical and numerical results in the analysis of the resonant frequency in the Eigenmode Solver.

As it is shown in table 3.2, between the analytical calculation and the numerical one there is an insignificant difference mainly due to the fact that the length of the pipes was neglected in the analytical calculation for simplicity.

To evaluate the resonant frequency in the Wakefield Solver it is necessary to analyze the transversal wake impedance. The latter is computed by the

[1] A different algorithm of meshing has been used and it is explained in details in paragraph 3.2.4

Mode	Eigenmode Solver (GHz)	Wakefield Solver (GHz)	High-frequency Solver (GHz)
TM_{010}	1.3106	1.3111	1.3122

Table 3.3: Comparison of the results in the analysis of the resonant frequency in different solvers.

Fourier-transformation of the transversal component of the wake potential, which is divided by the Fourier-transformed charge distribution function $\lambda(s)$:

$$Z_{\perp} = \frac{\int_{-\infty}^{\infty} W_{\perp}(s) e^{-j\omega s} ds}{\int_{-\infty}^{\infty} \lambda(s) e^{-j\omega s}} \tag{3.32}$$

Table 3.3 shows the result of the comparison of the result in the calculation of the resonant frequency in different solvers.

3.2.2 Quality Factor

The quality factor of a mode relates the stored energy to the energy loss during one RF period:

$$Q = \frac{\omega_0 W}{P} \tag{3.33}$$

For a cavity mode, where the electric and magnetic fields are 90° out of phase, the energy is continuously swapping between the magnetic energy and the electric energy such that, on average, the electric and magnetic stored energies are equal. The energy stored in a mode is given by:

$$W = W_E + W_M = \iiint \left(\frac{\varepsilon}{2} \mid E \mid^2 + \frac{\mu}{2} \mid H \mid^2 \right) dV \tag{3.34}$$

where the volume integral is to be extended over the entire cavity volume. On the other hand, a number of mechanisms can lead to energy loss in a cavity, but for a vacuum cavity, the dominating losses are ohmic losses in the not perfectly conducting walls. The tangential magnetic field near the metallic surface is equal to a surface current $\vec{J}_A = \vec{n} \times \vec{H}$ (in A/m, describing a current concentrated in the thin 'skin depth'). This surface current sees a surface resistance $R_A = \sqrt{\frac{\omega\mu}{2\sigma}}$ (in Ω), which will cause a small tangential voltage drop and thus resistive losses. To determine the total wall losses, this power density has to be integrated over the entire cavity surface to yield

$$P_{wall} = \frac{1}{2} \oiint_{wall} R_A \mid H_t \mid^2 dA \tag{3.35}$$

This is a perturbation method since we are assuming that the effect of the tangential voltage drop can be neglected compared to the dominating normal electric field of the mode. Note that the surface resistance $R_A =$ defined and used above is directly related to the skin depth δ via the formula:

$$\delta\sigma R_A = 1 \tag{3.36}$$

where σ is the conductivity of the surface wall material. Other loss mechanisms can readily be considered, e.g. losses in dielectric or magnetic materials inside the cavity, losses caused by radiation through openings, or even losses due to discharges inside the cavity. Also, the power lost through the main power coupler can be included. This latter is called the external Q (Q_{ext}). Since the power lost due to these different loss mechanisms must be added, the total resulting Q also referred to as Q_L (the loaded Q) is calculated from:

$$\frac{1}{Q_L} = \frac{P_{wall} + P_{ext} + ...}{\omega_0 W} = \frac{1}{Q_L} + \frac{1}{Q_{ext}} + \frac{1}{...} \tag{3.37}$$

A quantity often used is the coupling factor β that is the ratio P_{ext}/P_{wall}. Consequently, the loaded Q_L of the cavity is reduced from the unloaded Q by a factor $(1+\beta)^{-1}$:

$$Q_L = \frac{Q_0}{1+\beta} \tag{3.38}$$

The larger Q is, the less power will be needed to sustain stored energy inside the cavity. Similarly to the study of the resonance frequency, the Q factor was also analyzed both analytically and numerically for the modeled pill-box (see Tables 3.4 and 3.5). While the Eigenmode solver calculates the frequencies

Mode	CST Q-factor	Analytical Q-factor
TM_{010}	2.9714e3	2.9587e3
TM_{110}	3.6020e3	3.6111e3
TM_{210}	4.1554e3	4.2361e3

Table 3.4: Comparison between analytical and numerical results in the analysis of the Q factor in the Eigenmode Solver.

and the corresponding electromagnetic field patterns (eigenmodes) directly, in the wakefield solver the field monitors are necessary. The simulated wake length (WL) and the conductivity of the wall's material limit the calculation of the wakes to a certain distance WL from the source and plays an important role on the accuracy of the impedance results and in the duration of the simulation.

Mode	Eigenmode Solver	Wakefield Solver	High frequency Solver
TM_{010}	2.9714e3	2.9951e3	2.9376e3

Table 3.5: Comparison of the results in the analysis of the Q-factor in different solvers.

3.2.3 Shunt Impedance

Shunt impedance is a measure of the strength with which an eigenmode of a resonant radio frequency structure interacts with charged particles on a given straight line.

$$R = \frac{\mid V_{acc} \mid^2}{P} \tag{3.39}$$

Where V_{acc} is the accelerating voltage and P is the power dissipation. The accelerating voltage is defined as the integral of the axial electric field along the particle trajectory, taking the finite speed β of the particle into account:

$$V_{acc} = \int_{-\infty}^{\infty} E_z e^{j\frac{\omega z}{\beta c}} dz \tag{3.40}$$

The exponential term takes care of the fact that the field is varying while the particle is traversing the gap. The integral is extended here from $-\infty$ to $+\infty$ assuming that the beam tube diameter is small enough to form a wave guide well below its lowest cutoff at the resonance frequency ω, such that the fields extending from the cavity into the beam tube are rapidly decaying to zero. Maximizing the shunt impedance R allows optimization of the accelerating voltage that can be obtained for a given available power. Table 3.6 shows

Mode	Eigenmode Solver (Ω)	Wakefield Solver (Ω)
TM_{010}	2.0439e5	1.9841e5

Table 3.6: Comparison of the results in the analysis of the Shunt Impedance$R$ in different solvers.

the result of the comparison of the result in the calculation of the resonant frequency in different solvers.

3.2.4 Convergences study on mesh

CST Studio Suite offers a variety of meshes type and mesh generation algorithms, with the easy possibility of cross-verifying different methods and

meshes in the same GUI. The available numerical methods within the software include FIT (Finite Integration Technique) and TLM (Time Domain Solver) for the hexahedral meshing algorithm and FEM (Finite Element Method) for the tetrahedral one. Since the mesh influences the accuracy and speed of the simulation, so it is important to spend time in order to make the choice of the best-fitting solver. In general, hexahedral meshes are very robust even for most complex imported geometries, and in particular, the TLM solver offers a very efficient octree-based meshing algorithm which drastically reduces the overall cell count. Nevertheless, both FIT and TLM Hexahedral meshing algorithms do not conform to material jumps. On the other hand, CST tetrahedral meshes conform to solid-boundaries and consequently conform to material jumps. Moreover, adaptive mesh refinement schemes can be effectively applied to unstructured meshes, but their use may require special attention: sometimes inaccuracies of the CAD model will eventually interrupt the mesh generation. To control the mesh generation, there are different parameters that have either local or global influence on the mesh:

- Maximum Cell: the largest allowed cell size that is given by cells per wavelength or geometrical dimensions of the structure. The highest frequency of interest determines the smallest wavelength and thus dominates this value for high-frequency applications.
- Minimum Cell: the smallest allowed cell size that is defined as a fraction (ratio) from the maximum cell or as the absolute value.
- Refinement at PEC-edges: factor which determines how much finer the cells should be around PEC edges, which are known to have singular behavior of electric field values.

In fig.3.5 is possible to observe how the noise distortion is dramatically reduced using a number of cells per wavelength greater than 32.

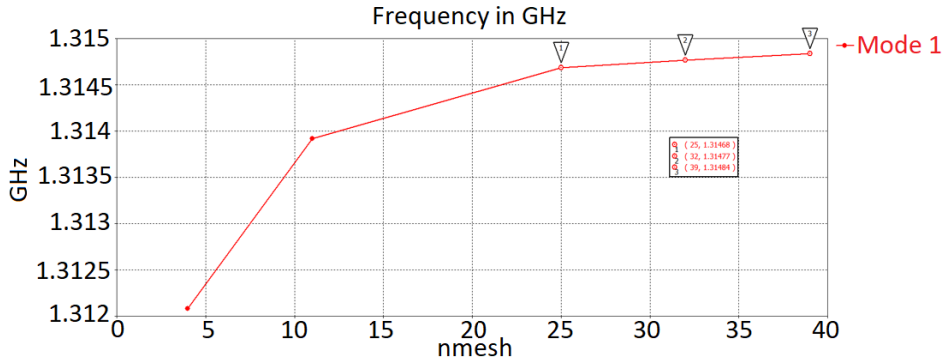

Figure 3.5: Convergences studies on the number of Maximum Cells per wavelength.

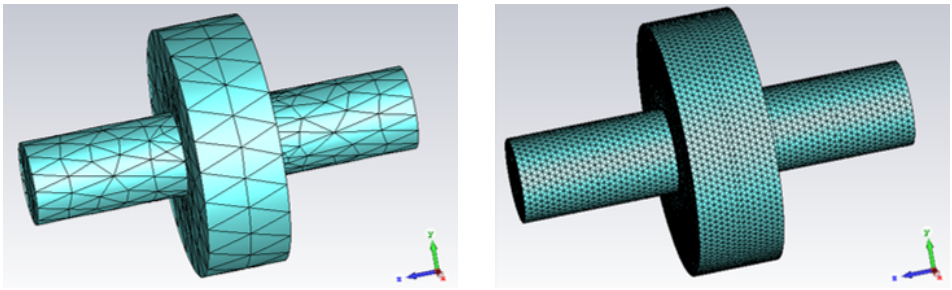

Figure 3.6: Tetrahedral Algorithm on a pill-box cavity. On the right 4 cells per wavelength, on the left 32 cells per wavelength.

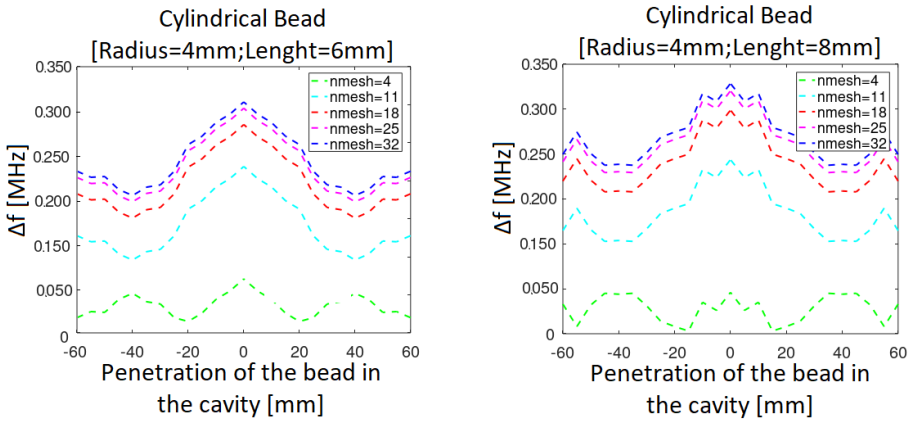

Figure 3.7: Simulated bead-pull method to implement convergences studies on the number of maximum cells per wavelength.

Fig. 3.6 shows the discretization of the used model in the first phase of the study with a value of 4 tetrahedral cells per wavelength and the discretization that has actually been implemented for the analysis on the numerical calibration of the bead pull method with a value of 32 cells per wavelength. Figure 3.7 shows the reason for this choice. As can be observed, increasing the number of cells is achieved a consistent convergency in the results of simulations.

3.3 Numerical Calibration of the Bead-Pull Method

As mentioned in paragraph 3.1, the bead-pull method is based on Slater's small signal perturbation theory which states that when a resonant cavity is perturbed by a small bead, the resonant frequency varies from the initial frequency and this change is proportional to the electric field. Shaped beads are used to enhance perturbation and give directional selectivity among different field components. For calibrated beads (knowing the bead constants) and controlled bead speed in the traversal of the structures, the bead-pull method allows a full characterization of resonances.
Once the cavity can be considered as known it's possible to start characterizing the bead implemented in the method. Its dimensions must be chosen so that the field does not vary significantly over its largest linear dimension and at the same time introduces a disturbance large enough to be distinguishable from the measurement noise. Two different forms of bead have been studied, spherical and cylindrical, depending on the respective parameters of radius (r) and length (l).

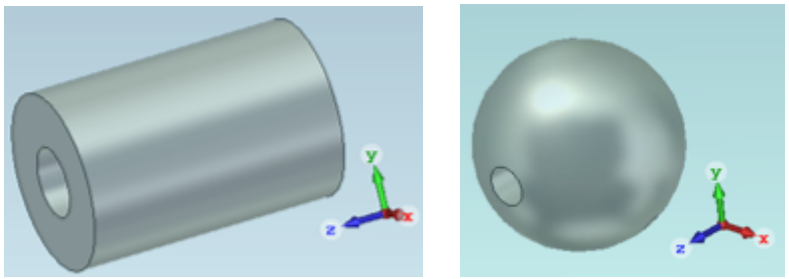

Figure 3.8: Bead modeled in the simulation.

Fig. 3.8 shows how the beads were modeled in the simulation. Despite the differences in shape and size, all have a central hole that represents the hole in which the wire of non-conductive material must be passed. Recalling

Eq.3.1 with the boundary condition whereby the magnetic field is zero along the center of the cavity is obtained:

$$\frac{\Delta\omega}{\omega_0} = \frac{\omega - \omega_0}{\omega_0} = -k_{SLE}\frac{|\ E\ |^2}{U} \tag{3.41}$$

The frequency shift of the resonance depends on the local electric and magnetic fields at the position of the perturbing object: the higher the field, the higher will be the frequency perturbation. An example of the frequency perturbation as a function of the longitudinal position for centered metallic beads in a circular pillbox cavity is displayed in Fig. 3.9: The mathematical

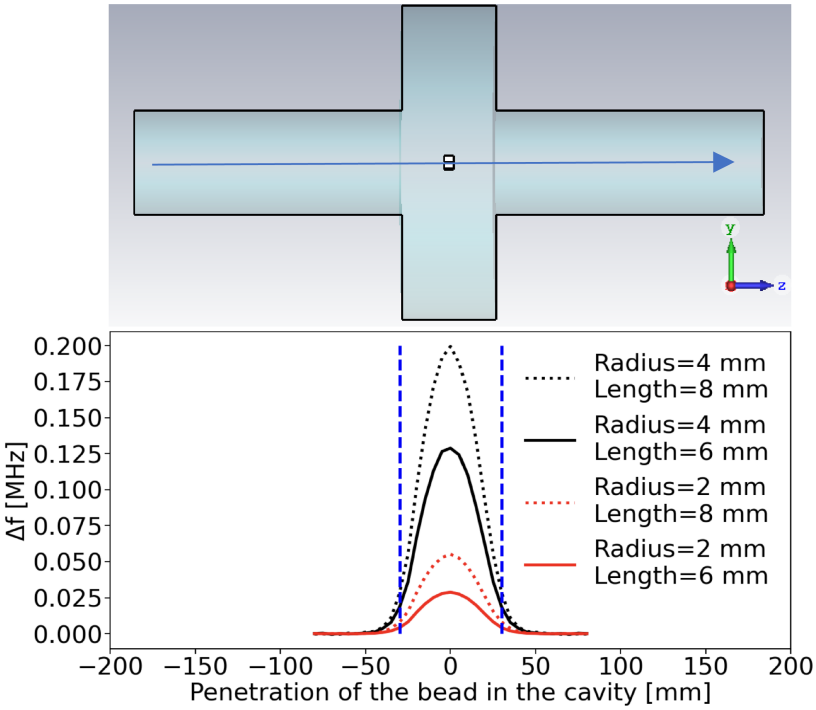

Figure 3.9: Top: longitudinal cross-section of the circular pillbox cavity simulated, in the center of the cavity a cylindrical bead is visible. Bottom: frequency perturbation of the TM_{010} mode for transversely centered beads having different lengths and radii as a function of the longitudinal position.

equation that describes the system together with Eq.3.41 is:

$$\frac{R}{Q_0} = \frac{V^2}{2\omega_0 U} \tag{3.42}$$

Eq. 3.42 describes the well-known ratio of R/Q that depends on the square of the electrical potential V, the original resonant angular frequency of the cavity ω_0 and the stored energy U. Rearrangement of Equations 3.41 and 3.42 gives:

$$\frac{V}{\sqrt{U}} = \int_0^L \sqrt{-\frac{\Delta\omega(z)}{k_{SLE}\omega_0}}dz \tag{3.43}$$

$$\frac{V}{\sqrt{U}} = \sqrt{\frac{2R\omega_0}{Q_0}} \tag{3.44}$$

That combined provide:

$$k_{SLE} = \frac{Q_0}{2R\omega_0}\left(\int_0^L \sqrt{-\frac{\Delta\omega(z)}{\omega_0}}dz\right)^2 \tag{3.45}$$

where the parameters ω_0, Q_0, R are obtained from eigenmode simulations on the reference circular pillbox cavity. The amplitude of the frequency perturbations obtained from simulations are displayed in Fig.3.10 and some values of the respective k_{SLE} are shown in Table 3.7 and in Table 3.8.[2]

Cylindrical Bead	$k_{SLE}{}^a$	$k_{SLE}{}^b$	Percentage Change
Radius=2mm Lenght=6mm	2.180e-4	2.658e-4	17.8%
Radius=3mm Lenght=6mm	4.121e-4	4.701e-4	12.3%
Radius=4mm Lenght=6mm	5.151e-4	5.677e-4	9.1%

Table 3.7: Values obtained from the calculation of the calibration constant for a cylindrical bead for cavities of different radius for the mode TM_{010}.

Tab. 3.7 shows the values of the calibration constant k_{SLE} obtained by simulating transversely centered cylindrical beads having different lengths and radii as a function of the longitudinal position, while Tab.3.8 displays the results for spherical beads having a different radius. In both cases, the error is found to be well below 20 %. This allows to conclude that for suitable dimensions of the bead the calibration in simulation is consistent.

[2]Since the amplitude of the perturbation depends only on the geometry of the perturbing object simulations have been performed for cavities with different radius:
[a] r=90 mm
[b] r=120 mm.

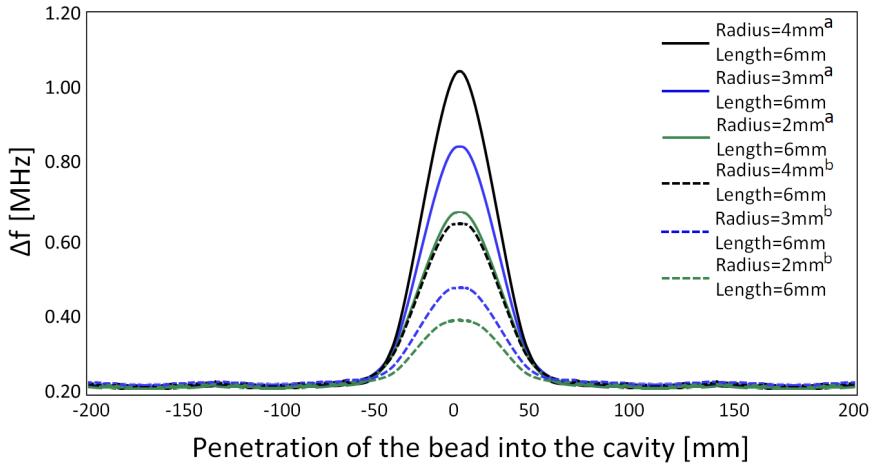

Figure 3.10: Frequency perturbation of the TM_{01} mode for transversely centered cylindrical beads having different lengths and radii as a function of the longitudinal position.

Spherical Bead	${k_{SLE}}^a$	${k_{SLE}}^b$	Percentage Change
Radius=2mm	3.005e-5	3.439e-5	12.6%
Radius=3mm	2.771e-5	3.104e-5	10.7%
Radius=4mm	4.552e-5	4.977e-5	8.5%

Table 3.8: Values obtained from the calculation of the calibration constant for a spherical bead for cavities of different radius for the mode TM_{010}.

To confirm the reliability of the method, the calibration of the beads was also studied for off-centered bead positions. In this case it must be underlined that the value of the shunt impedance has been calculated exactly where the bead is positioned (see Fig.3.11).

$$k_{SLE} = \frac{Q_0}{2\omega_0 R\mid_{x\,=x_t}} \left(\int_0^L \sqrt{-\frac{\Delta\omega(z)}{\omega_0}} dz \right)^2 \tag{3.46}$$

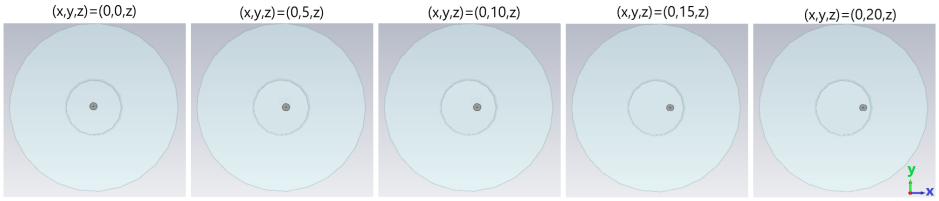

Figure 3.11: Transverse position of the bead into the cavity.

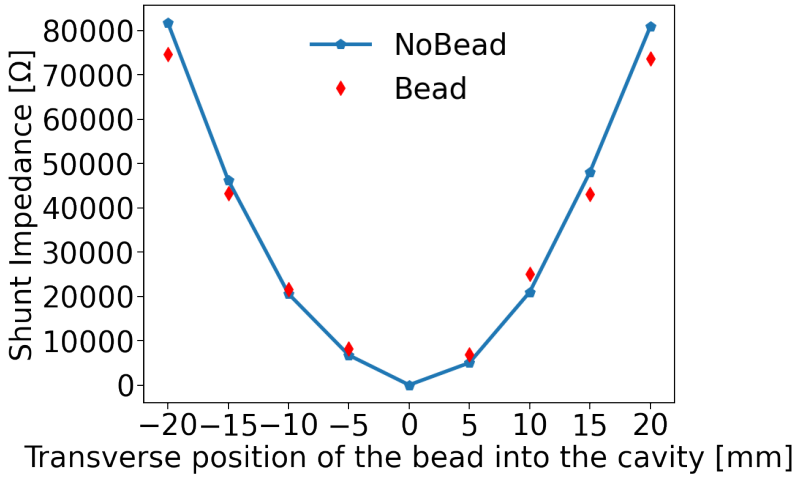

Figure 3.12: Comparison between the simulated longitudinal shunt impedance without the bead and the bead-pull numerical calibration method as a function of the transverse position of the bead.

Figure 3.12, as an example, shows a comparison between the simulated longitudinal shunt impedance obtained from CST eigenmode simulations without the bead and the bead-pull simulation technique for a calibrated bead obtained as a function of the transverse position of itself. The good agreement obtained shows the potential of the method for an accurate evaluation of the transverse beam coupling impedance. In fact, the transverse impedance can be obtained from the variation of the longitudinal impedance by using the Panofsky-Wenzel theorem as discussed in paragraph 2.2. Tab. 3.9 shows the values of the calibration constant k_{SLE} obtained by simulating cylindrical beads having different lengths and radii as a function of the longitudinal and transverse position.

k_{SLE}		Spehrical Bead		
		$r = 2mm$ $l = 6mm$	$r = 3mm$ $l = 6mm$	$r = 4mm$ $l = 6mm$
Trasverse Position of the bead	$pos_{xyz} = (0, 0, z)$	1.978e-4	3.22e-4	4.944e-4
	$pos_{xyz} = (0, 5, z)$	1.981e-4	3.292e-4	5.034e-4
	$pos_{xyz} = (0, 10, z)$	2.149e-4	3.332e-4	4.941e-4
	$pos_{xyz} = (0, 15, z)$	1.962e-4	3.288e-4	4.875e-4
	$pos_{xyz} = (0, 20, z)$	2.016e-4	3.377e-4	5.056e-4
Percentage Change		0.79≈7.9%	0.32≈2.8%	0.07≈12.5%

Table 3.9: Value of the calibration constant k_{SLE} of bead-pull method obtained as function of the transverse position of the bead.

Chapter 4

Direct benchmark of the measurement setup of the model with Eigenmode domain simulations

In order to assess the consistency of the calibration method, bead-pull measurements have been physically performed. The hardware of the Bead-Pull system consists of a:

- Pill-box like cavity with rectangular pipes that resonates at the frequency of $f_0 = 2.4255GHz$. The resonant structure is made of 316LN, nitrogen alloyed austenitic stainless steel with molybdenum addition while the pipes are made of Copper;
- Pulley system;
- Dielectric wire;
- Two spherical metallic beads ($D_1 = 2.48mm$, $D_2 = 3.05mm$)
- Antennas;
- Network analyzer: is a device that can measure the complex scattering parameters (S-parameters) in a broad range of frequencies (usually from kHz up to several GHz).
- Step Motor: consists of a permanent magnet rotating shaft called a rotor. The Step Motor converts digital pulses into mechanical shaft

rotation. Every rotation is divided into many discrete steps and it can stop at any step making it suitable for small movements. It has an excellent response to starting, stopping and reversing. However, it is hard to operate at high speeds and resonance can occur if not properly controlled.

- Arduino: Arduino is an open-source solution for developing electrical projects. It consists of a physical programmable circuit board, also known as a microcontroller, and software, known as IDE (Integrated Development Environment) [14], which is used to develop and upload computer code to the physical board. In the framework of this thesis, it has been used to set the parameters of the Step Motor, such as the velocity, the direction of movement, the acceleration rate and the deceleration rate.

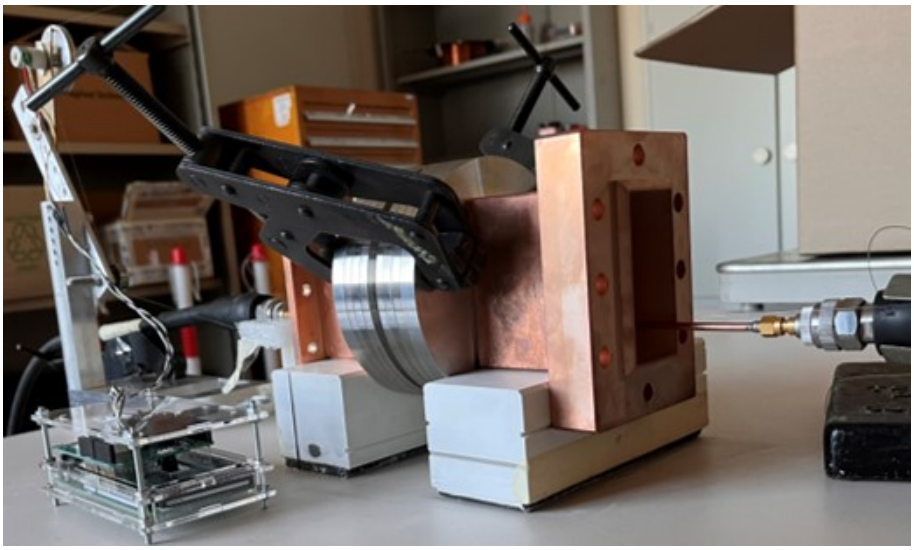

Figure 4.1: Pill-box like cavity with rectangular pipes where bead-pull measurements have been physically performed.

The bead-pull measurement setup is shown in Fig.4.1. The logic of the system is housed in the PC, which is running software to control the stepper motor drivers. The open-source Arduino software is used to execute the bead-pull measurements (IDE). A nylon wire is going longitudinally through the beam-pipe; it is organized in a closed loop and is powered by a motor linked to a pulley. A small metal or dielectric bead is then positioned on

this wire and is moved through the cavity perturbing the local distribution of the electric field. The latter is connected to the variation of resonance frequency, which is measured by the network analyzer in the form of phase shift. This data may be used to assess the tuning or field distribution of an RF resonant structure. A python script has been developed to analyze the measurement data.
During the first preliminary measurements a Variable voltage Power Supply (VVPS) has been used instead of the Arduino microcontroller to supply the step motor. Although, if properly calibrated, the results obtained between the two systems were congruent (as it is shown in Fig.4.2), the use of the VVPS introduces many degrees of uncertainty:

1. It was not possible to check the vibration of the wire;
2. It was not possible to set low speeds (necessary for small structures) due to the lower limit of the field of operability;
3. It was not possible to reverse the direction of movement except by manually reversing the polarization of the inputs.

Its use has however allowed to emphasize the critical aspects of the measurement system and to implement more efficiently the command file for the Arduino board.

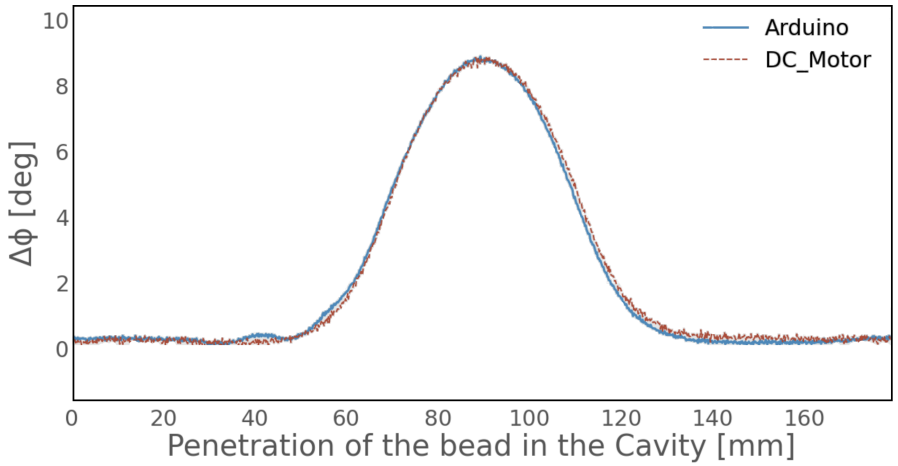

Figure 4.2: Comparison of the bead-pull technique obtain by a step motor supply by a microcontroller and a simpler DC source.

4.1 Bead-pull Measurements

The bead-pull measurement technique makes use of Slater's perturbation theorem, which links the bead to the frequency perturbation. Although the latter may be measured directly, it may be difficult to quantify it for minor fluctuations. As a result, it is interesting to detect the frequency shift indirectly, by measuring the phase shift of a transmitted signal at the resonance frequency [4]. The relationship between frequency shift and phase shift is given by:

$$\frac{\Delta\omega}{\omega_0} = \frac{1}{2Q_L}\tan\Delta\phi \tag{4.1}$$

where Q_L is the loaded quality factor, and $\Delta\phi$ is the phase shift in radians of the S_{21} transmission parameter at ω_0. Because of the non-linearity of the tan function, $\Delta\phi$ should be kept small enough (in practice, $\Delta\phi < 25°$) so that errors in the $\Delta\phi$ measurement do not lead to considerable errors in the frequency shift estimation.

As a first step, bead-pull measurements were performed for different positions of the measuring antenna inside the cavity. Since the method is itself already disruptive, the position of the antennas has been suitably studied in order not to introduce further distortions. Depending on how far the antennas penetrated into the pipes, the only thing that can vary to ensure the correct evaluation of the method is the module of the scattering parameter $\mid S_{21} \mid$ (see Fig.4.4). The position of the antennas affects (see Fig.4.3) the Q factor that is measured, in fact, the Q of a resonant circuit (in this case a resonant cavity) shows a sharp rise in gain over a narrow band centered at the resonant frequency f_R.

$$Q = \frac{\omega_0}{\omega_1 - \omega_2} \tag{4.2}$$

where ω_0 is the resonance frequency of the cavity, ω_1 is the upper $-3dB$ frequency, and ω_2 is the lower -3 dB frequency.
As explained below, in paragraph 3.2.2, Q may be defined as the ratio of the energy stored in the system to the energy dissipated per cycle, while ω_1 and ω_2 are often referred to as the half-power points. From the definition of the shunt impedance R of Eq.3.39, it is possible to obtain the power dissipated in the cavity as:

$$P = \frac{\mid V_{acc} \mid^2}{R} \tag{4.3}$$

Figure 4.3: Zoom on the positioning of the antenna inside the rectangular pipe of the pill-box like cavity involved in the bead-pull measurements.

If the power is halved, then:

$$\frac{P}{2} = \frac{\mid V_{acc} \mid^2}{2R} = \left(\frac{V_{acc}}{\sqrt{2}}\right)^2 \times \frac{1}{R} \tag{4.4}$$

Thus the power is halved when the voltage is divided by $\sqrt{2}$. Expressing this in dB:

$$20 \log_{10} \frac{1}{\sqrt{2}} = 20 \log_{10} 0.7071 = -3dB \tag{4.5}$$

Once the extremes of penetration of the antennas were defined, it was possible to proceed with real bead-pull measurements. Under this assumption of small perturbation, the frequency shift of the cavity resonance is given

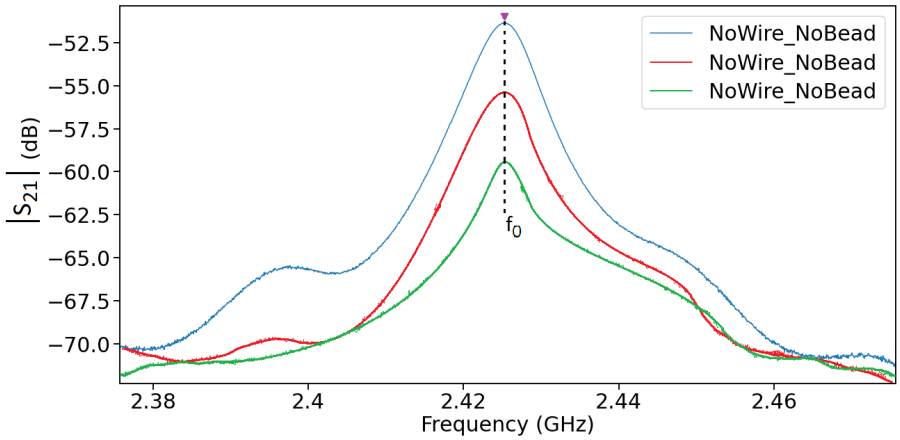

Figure 4.4: For different values of penetrations of the antennas into the pipes, the only thing that varies is the module of the scattering parameter $\mid S_{21} \mid$.

in an extended formula by:

$$\frac{\Delta\omega}{\omega_0} = \alpha_{E_\perp}\varepsilon_0\frac{\mid E_\perp \mid^2}{U} + \alpha_{E_\parallel}\varepsilon_0\frac{\mid E_\parallel \mid^2}{U} + \alpha_{H_\perp}\mu_0\frac{\mid H_\perp \mid^2}{U} + \alpha_{H_\parallel}\mu_0\frac{\mid H_\parallel \mid^2}{U} \quad (4.6)$$

where ε_0 and μ_0 are the vacuum permittivity and permeability, respectively; and $E_\perp$, $H_\perp$, $E_\parallel$ and $H_\parallel$ are the electric and magnetic fields perpendicular and parallel to the perturbing object. The coefficients $\alpha_{E_\perp}$, $\alpha_{H_\perp}$, $\alpha_{E_\parallel}$ and $\alpha_{H_\parallel}$ are the form factors associated to the respective fields, and they are proportional to the electric and magnetic polarizability of the perturbing object. Once the corresponding form factors are known, the absolute values of the measured electric and magnetic fields can be determined. Firstly, the electric field is directly obtained from the dielectric-sphere measurements. Secondly, the magnetic field is derived from metallic-sphere measurements. As a perturbing object, the sphere is chosen to measure the transverse components of the electromagnetic fields, both $E_\perp$ and $H_\perp$ due to its non-directional geometry. The perturbation effect becomes also non-directional as well.

$$\frac{\Delta\omega}{\omega_0} = -\pi r^3\varepsilon_0\frac{\mid E_\perp \mid^2}{U} + \frac{1}{2}\pi r^3\mu_0\frac{\mid H_\perp \mid^2}{U} \quad (4.7)$$

where r is the radius of the sphere. From Eq. 4.7, it is readily seen that a metallic sphere cannot distinguish between electric or magnetic fields separately, and the observed frequency shift will always be due to a combination

of both E and H. In order to be able to separate both components, a dielectric sphere need to be used. It will only interact with the electric field in the following way:

$$\frac{\Delta\omega}{\omega_0} = -\pi r^3 \frac{\varepsilon_r - 1}{\varepsilon_r + 2} \varepsilon_0 \frac{|\, E_\perp \,|^2}{U} \tag{4.8}$$

where ε_r is the relative permittivity of the material. Fig. 4.5 displays the bead-pull measurements of phase perturbation of the TM_{010} mode for transversely dielectric centered beads detected from antennas having different values of penetration inside the cavity pipes. The bead calibration already in simulation allows to choose the most suitable one depending on the purpose of the study. When using dielectric beads, for bead-pull measurements, it has the advantage of having three degrees of freedom: shape, dimension and material of the bead.

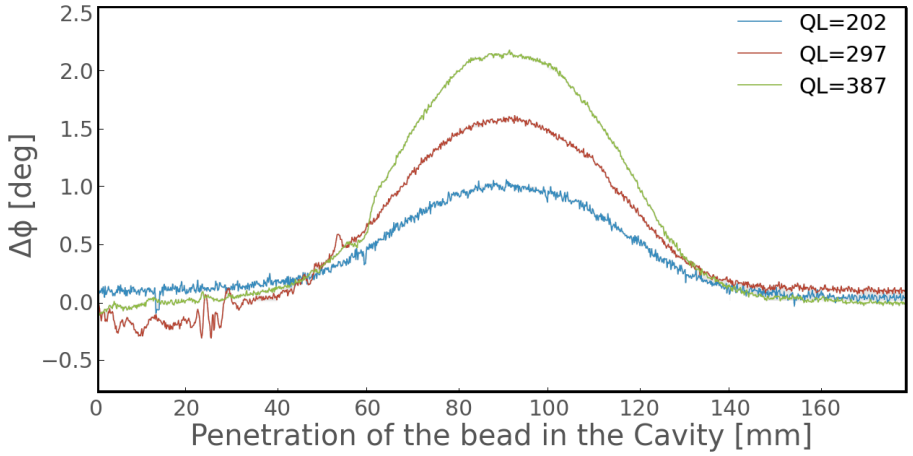

Figure 4.5: Measurements of phase perturbation of the TM_{010} mode for transversely dielectric centered beads detected from antennas having different value of penetration inside the cavity pipes.

The relative frequency variation is obtained from phase variation as from Eq. 4.1. and it is shown in Fig.4.6. We obtain:

$$\Delta f = \frac{\Delta\omega}{2\pi} = \frac{1}{2\pi} \frac{\omega_0}{2Q_L} \tan\Delta\phi \tag{4.9}$$

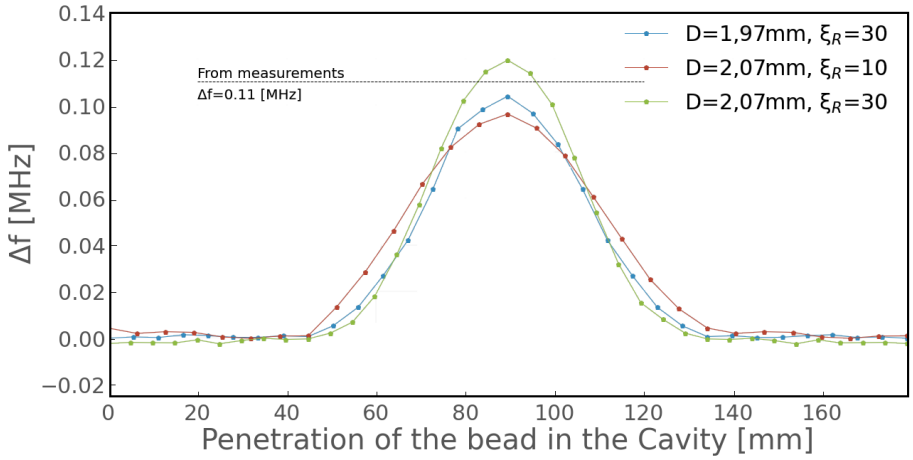

Figure 4.6: Simulation of frequency perturbation of the TM_{010} mode for transversely dielectric centered beads having different different values of the relative permittivity of the material.

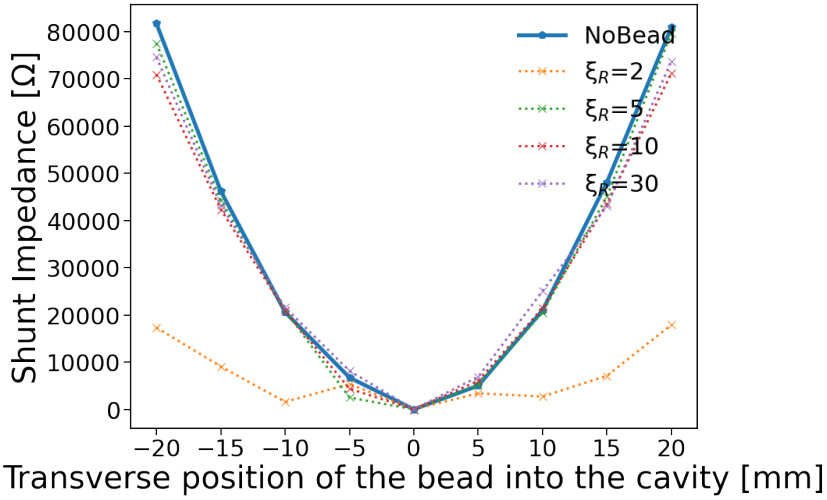

Figure 4.7: Characteristics of the shunt impedance of the cavity for different values of the relative permittivity of the material as obtained from simulations.

Fig. 4.7, as an example, shows a comparison between the simulated longitudinal shunt impedance obtained from CST eigenmode simulations for different values of the relative permittivity of the material. This graph gives

some preliminary information about the type of materials that should be preferred in order to achieve the most accurate results. Since the aim of this thesis is to develop a calibrated bead-pull method, the attention is focused on the bead itself and not on the distribution of the fields inside the cavity. Thus, measurements have been mostly taken with metallic beads.

The frequency shift shown in Fig.4.8 highlights the robustness of the method that for a given metallic bead independently of the value of the Q_L, i.e., penetration of the measuring antennas into the cavity, gives the same relative frequency perturbation.

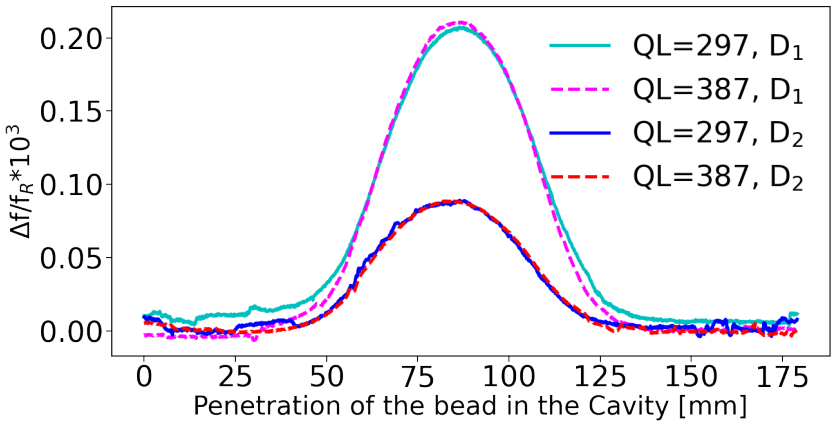

Figure 4.8: Relative variation of the resonant frequency as obtained from bead-pull measurements of $\Delta\phi$ and using Eq. 4.1 for two different loaded Q values and spherical metallic beads.

As a second step, CST eigenmode simulations of the DUT (see Fig. 4.10) have been performed considering a deviation of $100\mu m$ on the nominal value of radius of the beads. This has been represented with an error bar on the expected value of the frequency perturbation (see Fig.4.9). Measurements and simulations exhibit a reasonable agreement.

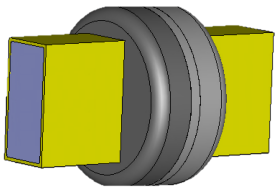

Figure 4.9: Virtual model of the cavity used in simulation.

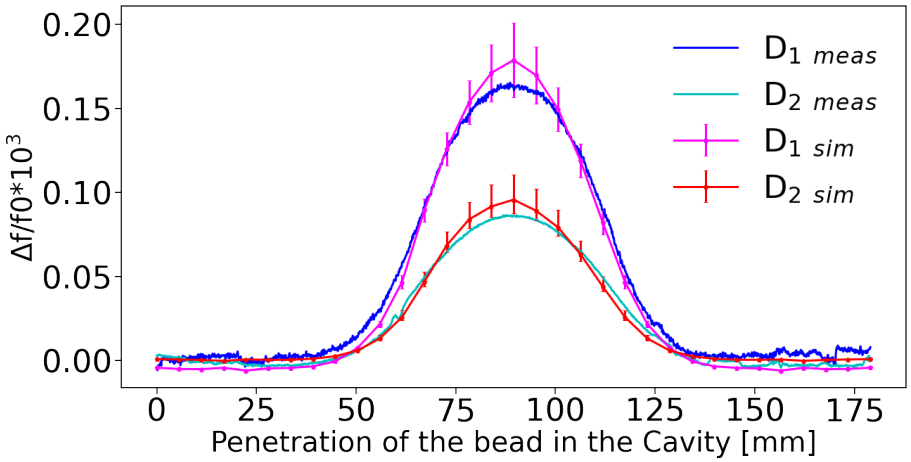

Figure 4.10: Comparison between measurements and simulations for metallic beads.

A lot of measurements have been performed in order to find the best parameters and therefore obtain a good agreement with the simulated results. Thus, a good database has been created. Unfortunately, some measurements will be totally unusable due to some mechanical/software problems with Arduino or the stepped motors.

As a final step to validate the virtual calibration method, the circular pillbox shown in Fig.3.9 has been adopted to obtain the calibration constant k_{SLE} for the beads used in the experimental setup. Therefore, by using Eq. 3.45 to calculate R, the impedance of the DUT is obtained by means of the Resonator Model:

$$Z = \frac{R}{1 = jQ_0\left(\frac{f}{f_0} - \frac{f_0}{f}\right)} \tag{4.10}$$

Figures 4.11 and 4.12 show the comparison between measurements and simulations respectively for the real and imaginary part of the impedance. The curves obtained with standard impedance simulations (without bead) are in very good agreement with the experimental measurements proving the high accuracy of the proposed calibration method for beam coupling impedance measurements.

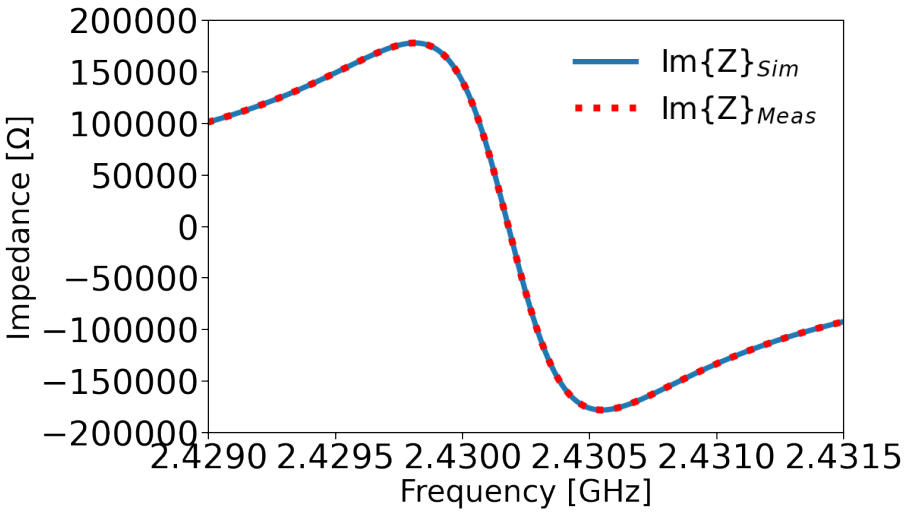

Figure 4.11: Zoom on the measurements performed with the 3.05 mm spherical metallic bead. Real part of DUT's impedance.

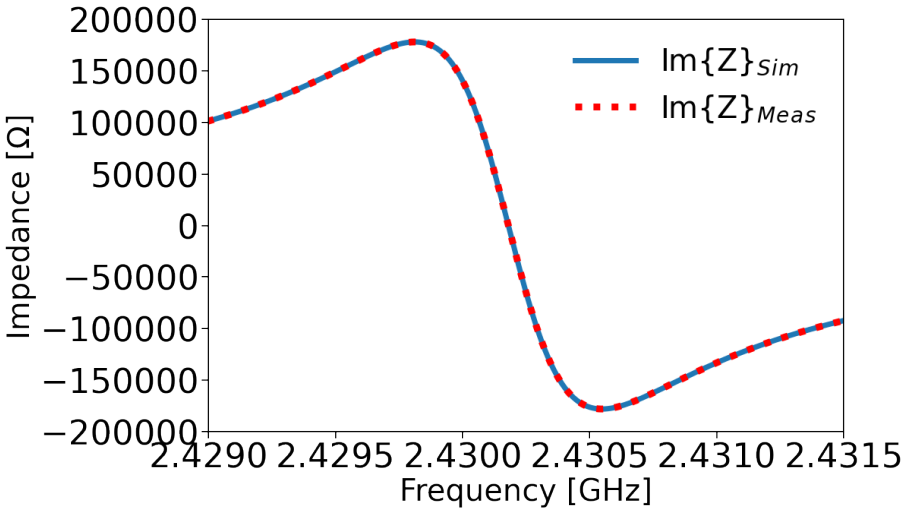

Figure 4.12: Zoom on the measurements performed with the 3.05 mm spherical metallic bead. Imaginary part of DUT's impedance.

Conclusion

In this master's thesis, the potential of the bead-pull method to perform beam coupling impedance measurements of cavity-like structures has been investigated. First of all, the available methods to compute the beam coupling impedance, have been discussed with a special focus on the Wire method (WM) and its limitations. In order to overcome these limitations, an alternative method, which does not require the modification of the DUT, has been proposed. The fundamental deflecting mode was originally studied using electromagnetic full-wave models. The bead-pull technique was used to measure the distinct components of the electric and magnetic fields where the transverse field components were measured using spheres made of various materials. A simulation procedure has been established for accurate calibration of the beads. A calibrated bead-pull configuration allows to measure the electric field and hence the shunt impedance of the cavity's resonant modes. The beam coupling impedance obtained with the calibrated bead-pull arrangement has been compared with well-established electromagnetic models. A good agreement between simulation and measurements has been found, confirming the reliability and accuracy of the measurement method.
In comparison to the conventional technique of measuring a reference cavity, the simulation method's flexibility in studying alternative bead shapes and sizes may be useful in optimizing the measurement setup. The bead calibration already in simulation allows to choose the most suitable one depending on the purpose of the study fully exploring the three degrees of freedom: shape, dimension and material of the bead. Moreover, since the magnitude of the perturbation for a particular electromagnetic field is solely determined by the geometry of the perturbing item, as evidenced several times in this document, calibration of the bead may be performed in a variety of resonant topologies without loss of generality.
The method has been experimentally validated for the derivation of the longitudinal beam coupling impedance and it has been shown to have potential also to measure the transverse beam coupling impedance.

Appendix

CAD Computer Aided Design

DUT Device Under Test

EM ElectroMagnetic

FD Frequency domain

FDTD Finite Differences Time Domain

FIT Finite Integration Technique

IDE Integrated Development Environment

k_{SLE} SLater Electric calibration constant

k_{SLE} SLater Magnetic calibration constant

LHC Large Hadron Collider

LW Lines per Wavelength

PS Particle Studio

REF Reference

RF Radio-Frequency

SPS Super Proton Synchrotron

TD Time Domain

TEM Transverse ElectroMagnetic

VNA Virtual Network Analyzer

VVPS Variable voltage Power Supply

WL Wake Length

WM Wire Method

Bibliography

[1] L.C.Maier and J.C. Slater. "Field Strength Measurements in Resonant Cavities". In: *Journal of Applied Physics* 23.1 (1952), p. 68.

[2] W.K.H. Panofsky and W.A. Wenzel. "Some considerations concerning the transverse deflection of charged particles in radio-frequency fields". In: *Sci. Instrum.* 27 (1956).

[3] A. Citron et al. *The Karlsruhe-CERN superconducting RF separator*. New York: Nucl. Instrum. Methods, 1979, p. 164.

[4] F. Caspers and G. Dôme. "Precise Perturbation Measurements of Resonant Cavities and Higher Order Mode Identification". In: *Proc. of Conference on Precision Electromagnetic Measurement*. Delft, The Netherlands, 1984, p. 4.

[5] R. L. Gluckstern and R. Li. *Analysis Of Coaxial Wire Measurement Of Longitudinal Coupling impedance*. Vol. 29. Particle Acccelerators, 1989, pp. 159–166.

[6] D. A. Edwards and M.J. Syphers. *An introduction to the physics of high energy accelerators*. Wiley, 1993.

[7] V.G.Vaccaro. "Coupling impedance measurements: an improved wire method". In: *Journal of Applied Physics* 23 (1994).

[8] B. W. Zotter and S. A. Kheifets. "Impedances and Wakes in High-Energy Particle Accelerators". In: *World Scientific* (1998).

[9] F. E. Close, F. Close, and M. Marten. *The Particle Odyssey: A Journey to the Heart of Matter*. 1st ed. New York: Oxford University Press, 2004, pp. 84–87.

[10] A. W. Chao, K. H. Mess, and M. Tigner. *Handbook of Accelerator Physics and Engineering*. 2nd ed. World Scientific., 2013.

[11] C. Zannini. "Electromagnetic Simulation of CERN Accelerator Components and Experimental Applications". PhD thesis. École polytechnique fédérale de Lausanne (EPFL), 2013.

[12] European Strategy Group. *2020 Update of the European Strategy for Particle Physics*. Geneve: CERN Council, 2020, p. 19.

[13] URL: https://www.simuleon.com/simulia-cst-studio-suite/.

[14] URL: https://www.arduino.cc/.